A numerical and experimental investigation of stability of natural convective flows within a horizontal annulus

By MARK P. DYKO[1], KAMBIZ VAFAI[1] AND A. KADER MOJTABI[2]

[1] Department of Mechanical Engineering, The Ohio State University, Columbus, OH 43210, USA

[2] IMFT-CNRS-INP/Universite Paul Sabatier, UMR 5502, 118 Route de Narbonne 31062, Toulouse Cedex, France

A numerical and experimental study of buoyancy-driven flow in the annulus between two horizontal coaxial cylinders at Rayleigh numbers approaching and exceeding the critical values is presented. The stability of the flow is investigated using linear theory and the energy method. Theoretical predictions of the critical Rayleigh number for onset of secondary flows are obtained for a wide range of radius ratio R and are verified by comparison with results of previous experimental studies. A subcritical Rayleigh number which provides a necessary condition for global flow stability is also determined. The three-dimensional transient equations of fluid flow and heat transfer are solved to study the manifestation of instabilities within annuli having impermeable endwalls, which are encountered in various applications. For the first time, a thorough examination of the development of spiral vortex secondary flow within a moderate gap annulus and its interaction with the primary flow is performed for air. Simulations are conducted to investigate factors influencing the size and number of post-transitional vortex cells. The evolution of stable three-dimensional flow and temperature fields with increasing Rayleigh number in a large gap annulus is also studied. The distinct flow structures which coexist in the large gap annulus at high Rayleigh numbers preceding transition to oscillatory flow, including transverse vortices at the end walls which have not been previously identified, are established numerically and experimentally. The solutions for the large-gap annulus are compared to those for the moderate-gap case to clarify fundamental differences in behaviour. Heat transfer results in the form of local Nusselt number distributions are presented for both the moderate- and large-gap cases. Results from a series of experiments performed with air to obtain data for validation of the numerical scheme and further information on the flow stability are presented. Additionally, the change from a crescent-shaped flow pattern to a unicellular pattern with centre of rotation at the top of the annulus is investigated numerically and experimentally for a Prandtl number of 100. Excellent agreement between the numerical and experimental results is shown for both Prandtl numbers studied. The present work provides, for the first time, quantitative three-dimensional descriptions of spiral convection within a moderate-gap annulus containing air, flow structures preceding oscillation in a large-gap annulus for air, and unicellular flow development in a large-gap annulus for large Prandtl number fluids.

1. Introduction

Linear and nonlinear stability of the Rayleigh–Bénard problem have been the subject of numerous publications. Owing to the difficulty in solving the natural convection equations in an annular layer, however, only a few stability studies have been performed. Mojtabi & Caltagirone (1979) studied the stability of the two-dimensional flow using a perturbation method. The solution was restricted to the upper part of the annular layer and to small values of Rayleigh number and R owing to the approximation of the real solution by a power series expansion of Rayleigh number up to the second order. Walton (1980) conducted a stability analysis of natural convection flow in an annulus of small R by employing a WKB formulation for the perturbed solution. He showed that for a Prandtl number greater than 0.24 the onset of instability occurs at the top of the annulus and is therefore thermal in nature, whereas for a Prandtl number below 0.24 the instability can occur elsewhere, indicating that it originates in part owing to hydrodynamic influences. Choi & Kim (1993) conducted a linear stability analysis of two-dimensional flow of air between horizontal cylinders. For other than very small Prandtl numbers, only a few numerical studies of post-transitional flow in a horizontal annulus have been published. In nearly all of these studies, a two-dimensional model was employed (Powe, Carley & Carruth 1971; Fant, Rothmayer & Prusa 1991; Cheddadi *et al.* 1992; Yoo 1996) and therefore neither the spiral secondary flows which are observed experimentally in annuli of moderate R nor the influence of solid endwalls which bound a finite-length annulus could be analysed. Rao *et al.* (1985) carried out steady three-dimensional calculations for a case of moderate R. However, only a fluid with Prandtl number of 5000 was studied which limits the range of practical applicability of their results. It was therefore of interest to extend the previous studies of linear and nonlinear stability by using numerical models to explore both critical and subcritical instabilities over a wide range of R, and to investigate secondary flow and thermal fields within an air filled annulus of moderate R including the effects of the solid endwalls, which requires a three-dimensional model.

While the topic of natural convection between horizontal coaxial cylinders has been widely studied owing to its many practical applications, most of the previous numerical work has dealt with two-dimensional flow in a long annulus. Three-dimensional laminar flow within a horizontal annulus of large R which arises owing to the presence of impermeable endwalls has only recently been investigated. Takata *et al.* (1984) studied the effects of annulus inclination for a fluid with Prandtl number of 5000. Their results revealed the existence of a coaxial double helical flow pattern adjacent to each endwall caused by the viscous shearing effects of the endwalls. For the horizontal case, the flow had a relatively small component of axial velocity. Fusegi & Farouk (1986) analysed three-dimensional natural convection in an air filled annulus of small axial length. Double helical flow patterns qualitatively similar to those reported by Takata *et al.* (1984) were calculated. Vafai & Ettefagh (1991) conducted a transient numerical analysis of the formation of three-dimensional flow and temperature fields. Their results showed that in the mid-axial region of the annulus the temperature distribution remains unchanged and the flow is nearly two-dimensional, provided the length to outer radius ratio is sufficiently large. A numerical investigation of two- and three-dimensional turbulent natural convection in a horizontal annulus was conducted by Desai & Vafai (1994). In the present work, the development and structure of three-dimensional laminar flows which precede transition to oscillatory instability in an annulus of large R are examined for the first time. Similarities and differences compared to convection in an annulus of moderate R are illustrated for a

Prandtl number of 0.7. In addition, experimental and numerical results are presented showing the unicellular flow development leading up to transition to turbulence in an annulus of large R for large Prandtl numbers, for which a three-dimensional analysis has not been previously conducted.

Numerous experimental studies have been carried out to obtain quantitative information about the *global* heat transfer within a horizontal annulus. The results were presented by a correlation between the Nusselt number and the Rayleigh number, Prandtl number, and R (Liu, Mueller & Landis 1961). Other studies revealed different convective regimes, especially that of Grigull & Hauf (1966), who used a Mach–Zehnder interferometer for their visualizations. Powe *et al.* (1969) showed the existence of four convective regimes in an annulus containing air: a unicellular two-dimensional steady regime for small Rayleigh number and any value of R, a multicellular regime for higher Rayleigh numbers and $R < 1.24$, a spiral flow regime for R between 1.24 and 1.71, and an oscillating regime for very high Rayleigh number and $R > 1.71$. A multicellular regime was previously observed for $R = 1.15$ by Liu *et al.* (1961). According to these authors, the onset of this regime is due to the fact that the critical Rayleigh number of 1708 was exceeded in the horizontal layer formed locally by the upper part of the annulus. This interpretation is confirmed here by a stability study. All of the experimental studies carried out by various authors clearly demonstrate the onset of secondary flows accompanying the primary unicellular flow for relatively high Rayleigh numbers.

In the present study, the linear stability of this steady two-dimensional flow and the nonlinear stability, using the energy method, are investigated. The basic two-dimensional flow is determined by a numerical model using the ADI method. In the three-dimensional numerical investigation, the governing equations are formulated in terms of vorticity and vector potential. The parabolic equations are solved by a three-dimensional ADI method and the elliptic equations are solved by the extrapolated Jacobi scheme. The two-dimensional numerical results and, for the case of a long annulus in which the characteristics of two-dimensional flow are present at the mid-axis, the three-dimensional numerical results closely agree with those obtained by Kuehn & Goldstein (1976). Excellent agreement of the three-dimensional numerical solutions with results of the current experimental studies is shown. The stability study enables us to define criteria for the onset of the secondary flows observed experimentally. Through the numerical computations and experiments, the manifestation of thermal instability as a transition from two- to three-dimensional flow and the effects of Rayleigh number and annulus geometry on the flow and thermal fields are elucidated.

2. Formulation and solution

2.1. *Three-dimensional flow*

The horizontal coaxial cylinders with inner and outer radii r_i and r_o are maintained at temperatures T_i and T_o, respectively, with $T_i > T_o$. The annulus is of length l and the two axial ends are impermeable and adiabatic. The geometrical configuration, characterized by the radius ratio $R = r_o/r_i$, is shown in figure 1. The dimensionless length is defined as $L = l/r_i$. As observed experimentally in the present work and in previous studies such as that by Grigull & Hauf (1966), the flow is symmetric about the vertical plane passing through the axis of the cylinders (angular symmetry plane) for the various combinations of R and Rayleigh number considered in the present numerical study. The computational domain was therefore chosen to encompass $0 \leqslant \phi \leqslant \pi$. This point was also confirmed through numerical experimentation.

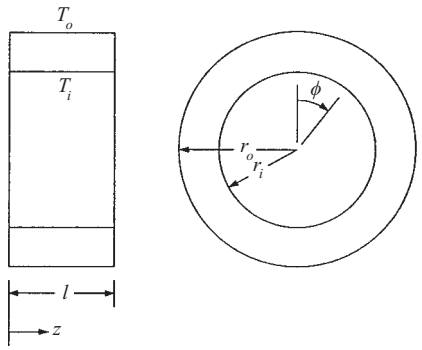

FIGURE 1. Schematic diagram of the horizontal annulus.

The three-dimensional, transient, laminar, buoyancy-induced flow of an incompressible fluid is governed by the equations of conservation of mass, momentum, and energy, which are simplified using the Boussinesq approximation. The components of the gravitational vector in the r, ϕ, and z directions are $-g\cos\phi\boldsymbol{e}_1$, $g\sin\phi\boldsymbol{e}_2$, and 0, respectively, where g is the acceleration due to gravity and the unit vectors in cylindrical coordinates are $\boldsymbol{e}_1$, $\boldsymbol{e}_2$, and $\boldsymbol{e}_3$. By taking the curl of the momentum equation, the pressure term is eliminated, yielding the vorticity transport equations

$$\frac{\partial\Omega_r}{\partial r}+(\boldsymbol{V}\cdot\boldsymbol{\nabla})\,\Omega_r-(\boldsymbol{\Omega}\cdot\boldsymbol{\nabla})\,V_r=Pr\left(\nabla^2\Omega_r-\frac{\Omega_r}{r^2}-\frac{2}{r^2}\frac{\partial\Omega_\phi}{\partial\phi}\right)+Pr\,Ra_r\sin\phi\frac{\partial\Theta}{\partial z},\tag{1}$$

$$\frac{\partial\Omega_\phi}{\partial t}+(\boldsymbol{V}\cdot\boldsymbol{\nabla})\,\Omega_\phi-(\boldsymbol{\Omega}\cdot\boldsymbol{\nabla})\,V_\phi+\frac{V_\phi\Omega_r-V_r\Omega_\phi}{r}$$
$$=Pr\left(\nabla^2\Omega_\phi-\frac{\Omega_\phi}{r^2}+\frac{2}{r^2}\frac{\partial\Omega_r}{\partial\phi}\right)+Pr\,Ra_r\cos\phi\frac{\partial\Theta}{\partial z},\tag{2}$$

$$\frac{\partial\Omega_z}{\partial t}+(\boldsymbol{V}\cdot\boldsymbol{\nabla})\,\Omega_z-(\boldsymbol{\Omega}\cdot\boldsymbol{\nabla})\,V_z=Pr\,\nabla^2\Omega_z-Pr\,Ra_r\left(\sin\phi\frac{\partial\Theta}{\partial r}+\frac{1}{r}\cos\phi\frac{\partial\Theta}{\partial\phi}\right),\tag{3}$$

where the vorticity vector is defined as

$$\boldsymbol{\Omega}=\boldsymbol{\nabla}\times\boldsymbol{V}.\tag{4}$$

To calculate the velocity field from the vorticity field, the vector potential $\boldsymbol{\Psi}$ is introduced

$$\boldsymbol{V}=\boldsymbol{\nabla}\times\boldsymbol{\Psi}.\tag{5}$$

Note that the equation of continuity is satisfied automatically by this expression. From equations (4) and (5) and assuming a solenoidal solution of $\boldsymbol{\Psi}$, i.e. $\boldsymbol{\nabla}\cdot\boldsymbol{\Psi}=0$, the following equation relating vector potential and vorticity is obtained

$$-\boldsymbol{\Omega}=\nabla^2\boldsymbol{\Psi}.\tag{6}$$

Equation (6) is written as

$$-\Omega_r=\nabla^2\Psi_r+\frac{2}{r}\frac{\partial\Psi_r}{\partial r}+\frac{\Psi_r}{r^2}+\frac{2}{r}\frac{\partial\Psi_z}{\partial z},\tag{7}$$

$$-\Omega_\phi=\nabla^2\Psi_\phi-\frac{\Psi_\phi}{r^2}+\frac{2}{r^2}\frac{\partial\Psi_r}{\partial\phi},\tag{8}$$

$$-\Omega_z=\nabla^2\Psi_z.\tag{9}$$

From equation (5), the components of dimensionless velocity are

$$V_r = \frac{1}{r}\frac{\partial \Psi_z}{\partial \phi} - \frac{\partial \Psi_\phi}{\partial z}, \tag{10}$$

$$V_\phi = \frac{\partial \Psi_r}{\partial z} - \frac{\partial \Psi_z}{\partial r}, \tag{11}$$

$$V_z = \frac{\Psi_\phi}{r} + \frac{\partial \Psi_\phi}{\partial r} - \frac{1}{r}\frac{\partial \Psi_r}{\partial \phi}. \tag{12}$$

Equations (1)–(3) and (7)–(12), along with the energy equation (13), are the final form of the non-dimensional governing equations.

$$\frac{\partial \Theta}{\partial t} + (\boldsymbol{V}\cdot\boldsymbol{\nabla})\,\Theta = \nabla^2\Theta. \tag{13}$$

The reference quantities used in non-dimensionalization of the conservation equations are r_i for length, α/r_i for velocity, r_i^2/α for time and $\rho\alpha^2/r_i^2$ for pressure, with α and ρ denoting the thermal diffusivity and density, respectively. The dimensionless temperature is defined by $\Theta = (T - T_o)/\Delta T$, where $\Delta T = T_i - T_o$, and the dimensionless parameters Rayleigh number Ra_r and Prandtl number Pr are defined as

$$Ra_r = \frac{g\beta r_i^3 \Delta T}{\alpha\nu}, \quad Pr = \frac{\nu}{\alpha}, \tag{14}$$

where β is the coefficient of thermal expansion and ν the kinematic viscosity.

The annulus inner and outer cylinders are maintained at dimensionless temperatures $\Theta = 1$ and $\Theta = 0$, respectively. At the surfaces of the cylinders, the components of velocity are zero and the components of vorticity follow from equation (4). The vector potential boundary conditions are in accordance with the work of Hirasaki & Hellums (1968), with the normal gradient of the normal component of vector potential specified as zero and the components of vector potential tangential to the surface also being zero. The dimensionless boundary conditions at $r = 1$ and $r = R$ are therefore

$$V_r = V_\phi = V_z = 0, \tag{15}$$

$$\Omega_r = 0, \quad \Omega_\phi = -\frac{\partial V_z}{\partial r}, \quad \Omega_z = \frac{\partial V_\phi}{\partial r}, \tag{16}$$

$$\frac{\partial}{\partial r}(r\Psi_r) = \Psi_\phi = \Psi_z = 0, \tag{17}$$

$$\Theta = 1 \quad \text{at} \quad r = 1, \tag{18}$$

$$\Theta = 0 \quad \text{at} \quad r = R. \tag{19}$$

Since there is no fluid flow or heat conduction across the angular symmetry plane, the normal component of velocity and the normal gradient of temperature are zero. The normal gradients of the tangential velocity components are also zero. At $\phi = 0$ and $\phi = \pi$

$$\frac{\partial V_r}{\partial \phi} = V_\phi = \frac{\partial V_z}{\partial \phi} = 0, \tag{20}$$

$$\Omega_r = \frac{\partial \Omega_\phi}{\partial \phi} = \Omega_z = 0, \tag{21}$$

$$\Psi_r = \frac{\partial \Psi_\phi}{\partial \phi} = \Psi_z = 0, \tag{22}$$

$$\frac{\partial \Theta}{\partial \phi} = 0. \tag{23}$$

The three components of velocity and the normal gradient of temperature are zero at the impermeable, adiabatic endwalls of the annulus. Therefore, at $z = 0$ and $z = L$

$$V_r = V_\phi = V_z = 0, \tag{24}$$

$$\Omega_r = -\frac{\partial V_\phi}{\partial z}, \quad \Omega_\phi = \frac{\partial V_r}{\partial z}, \quad \Omega_z = 0, \tag{25}$$

$$\Psi_r = \Psi_\phi = \frac{\partial \Psi_z}{\partial z} = 0, \tag{26}$$

$$\frac{\partial \Theta}{\partial z} = 0. \tag{27}$$

The system of nonlinear governing equations (1)–(3), (7)–(12), and (13) is solved by first advancing the energy equation (13) and vorticity equations (1)–(3) in time using a modified form of the three-dimensional alternating direction implicit (ADI) method developed by Brian (1961). The vector potential equations (7)–(9) are then iterated to convergence using the extrapolated Jacobi method with optimum over-relaxation parameter. Velocities are subsequently calculated via central difference approximations to equations (10)–(12). The updated values are used in the next timestep and the entire sequence is repeated. At each time level, convergence to steady state is checked by calculating the relative changes of the temperature, vorticity components, and vector potential components at every mesh point and comparing these to a prescribed constant, which was set to 10^{-3}. Steady state is assumed to have been achieved when

$$\frac{\xi^{n+1}_{i,j,k} - \xi^{n}_{i,j,k}}{\xi^{n}_{i,j,k}} \leqslant 10^{-3}, \tag{28}$$

where n is a particular time level and ξ is any one of the dependent variables.

In the numerical simulations the inner and outer cylinders, adiabatic endwalls, and fluid between the cylinders are assumed to be initially at the same uniform temperature of $\Theta = 0$, and the fluid is assumed to be initially stationary throughout the annular space. The temperature of the inner cylinder is suddenly increased to $\Theta = 1$ at $t = 0$, and the flow patterns which subsequently develop do so naturally as a result of transient heating of the fluid. Aside from being quite basic, these conditions are representative of actual applications. One of the primary objectives of the numerical investigation was to analyse three-dimensional flow and temperature distributions in moderate-gap annuli at Rayleigh numbers above and below the critical value for onset of secondary flows. Another was to study the evolution of three-dimensional flow and temperature distributions with increasing Rayleigh number in larger-gap annuli, for which the present stability analysis is not valid. For the cases studied, steady flow behaviour was calculated to occur after a sufficient period of time had elapsed, which is in agreement with experimental results.

The mean Nusselt number is defined as the angular average of the local Nusselt number at the mid-axial plane, where the local Nusselt number is the ratio of the actual to conduction heat transfer. The expressions for the inner and outer cylinder mean Nusselt numbers $\overline{Nu}_i$ and $\overline{Nu}_o$, respectively, are

$$\overline{Nu}_i = \frac{-1}{\pi}\int_0^{\pi} \ln(R)\left.\frac{\partial \Theta}{\partial r}\right|_{r=1} \mathrm{d}\phi, \tag{29}$$

$$\overline{Nu}_o = \frac{-1}{\pi}\int_0^{\pi} R\ln(R)\left.\frac{\partial \Theta}{\partial r}\right|_{r=R} \mathrm{d}\phi. \tag{30}$$

2.2. *Two-dimensional reference state*

In order to investigate the stability of the basic solution and define the critical conditions for onset of three-dimensional phenomena, it is necessary to define the reference state by the temperature and velocity fields. For small values of Rayleigh number a steady two-dimensional regime sets in with a vertical symmetry plane. Consequently, for computational efficiency the reference state was obtained by solving the two-dimensional vorticity, stream function, and energy equations. These are reduced from the full three-dimensional equations by setting the z-velocity and gradients of the variables in the z-direction equal to zero, thereby eliminating the axial dependency. The system of equations was solved by the ADI method. For small Rayleigh numbers and for air, the flow regime observed experimentally and calculated by the two- and three-dimensional numerical models is a symmetric unicellular one. In what follows, the stability of this flow is analysed.

3. Linear stability

The stability study is based on the Galerkin method. The results of the numerical model are successively used to define the initial state on which infinitely small temperature, pressure, and velocity perturbations are superposed. The purpose here is to determine the critical values of the Rayleigh number as a function of the radius ratio, at which this two-dimensional basic flow becomes three-dimensional.

3.1. *Linear stability with regard to axisymmetrical perturbations near* $\phi = 0$

The velocity, temperature, and pressure fields V^*, Θ^*, and P^* are decomposed as

$$V^* = V + \boldsymbol{v},$$
$$\Theta^* = \Theta + \theta,$$
$$P^* = P + p,$$

where V, Θ, and P represent the basic two-dimensional flow and $\boldsymbol{v}$, θ, and p represent the disturbance fields. According to previous experimental studies, the assumption that the perturbations appear only in the upper part of the annular layer is made. Thus the two-dimensional perturbations are developed in a periodical form in z

$$\boldsymbol{v} = [v_r(r,t)\,\boldsymbol{e}_1 + v_z(r,t)\,\boldsymbol{e}_3]\exp(\mathrm{i}sz), \tag{31}$$

$$\theta = \theta(r,t)\exp(\mathrm{i}sz), \tag{32}$$

where $s = m\pi r_i/l$ is the wavenumber and m the number of cells developed over the length l. Setting the perturbed fields to satisfy the governing mass, momentum, and

	$N=1$		$N=2$		$N=3$	
R	Ra_c	S_c	Ra_c	S_c	Ra_c	S_c
			Linear theory			
1.2	1769.86	3.131	1728.22	3.132	1727.47	3.132
$2^{1/2}$	1848.26	3.171	1804.87	3.173	1804.21	3.173
2	2095.71	3.171	2046.98	3.322	2047.02	3.322
			Energy method			
1.2	1753.72	3.122	1712.16	3.122	1711.38	3.122
$2^{1/2}$	1788.7	3.137	1746.66	3.137	1745.94	3.137
2	1826.54	3.183	1783.77	3.184	1783.12	3.184

TABLE 1. Critical Rayleigh number and wavenumber obtained by the linear theory and energy method for $R = 1.2$, $2^{1/2}$, and 2 with $Pr = 0.7$ and with approximations $N = 1, 2, 3$

energy equations, neglecting the second-order terms, and taking the curl of the momentum equation results in the equations of the marginal state

$$\sum_{k=1}^{N} a_k \left\langle \theta_l \mathscr{L}(\theta_k) + \frac{\theta_l \theta_k}{r^2} - \theta_l V_r \frac{\partial \theta_k}{\partial r} \right\rangle - b_k \left\langle \theta_l v_{rk} \frac{\partial \Theta}{\partial r} \right\rangle = 0, \tag{33}$$

$$\sum_{k=1}^{N} Ra_r Pr\, a_k \left\langle v_{rl} \left(\frac{1}{r} \frac{\partial \theta_k}{\partial r} - s^2 \theta_k \right) \right\rangle + b_k \left\langle Pr\, v_{rl} \mathscr{L}^2(v_{rk}) - \frac{v_{rl}}{r^2} \frac{\partial}{\partial r} (r^2 v_{rk} \nabla_r^2 V) - v_{rl} \frac{\partial}{\partial r} (V_r \mathscr{L}(v_{rk})) \right\rangle = 0, \tag{34}$$

where the operator $\mathscr{L}$ is defined by

$$\mathscr{L} = \mathrm{D}^2 + \frac{\mathrm{D}}{r} - s^2 - \frac{1}{r^2}, \quad \text{where } \mathrm{D} = \frac{\mathrm{d}}{\mathrm{d}r}$$

and $\mathscr{L}^2$ is defined by

$$\mathscr{L}^2 = \mathrm{D}^4 + \frac{2\mathrm{D}^3}{r} - \left(2s^2 + \frac{3}{r^2}\right)\mathrm{D}^2 - \left(\frac{2s^2}{r} - \frac{3}{r^3}\right)\mathrm{D} + \left(s^2 + \frac{1}{r^2}\right)^2 - \frac{4}{r^4},$$

and

$$\nabla_r^2 V = \frac{\partial}{\partial r}\left(\frac{1}{r}\frac{\partial}{\partial r}(rV_r)\right) + \frac{1}{r^2}\frac{\partial^2 V_r}{\partial \phi^2} - \frac{2}{r^2}\frac{\partial V_\phi}{\partial \phi}$$

$$\langle \zeta \rangle = \int_1^R \zeta \, \mathrm{d}r,$$

and where the perturbations used for θ and v_r are

$$\theta = \sum_{k=1}^{N} a_k \theta_k(r), \quad v_r = \sum_{k=1}^{N} b_k v_{rk}(r).$$

It is difficult to calculate various integrals in equations (33) and (34) involving V_r, V_ϕ, and Θ and their partial derivatives, thus the polynomial giving the best approximation for each expression of the basic flow is obtained before calculating the integrals for $\phi = 0$. Equations (33) and (34) represent an algebraic system with $2N$ equations and $2N$ variables made up of the terms a_k and b_k where $k \in [1, N]$.

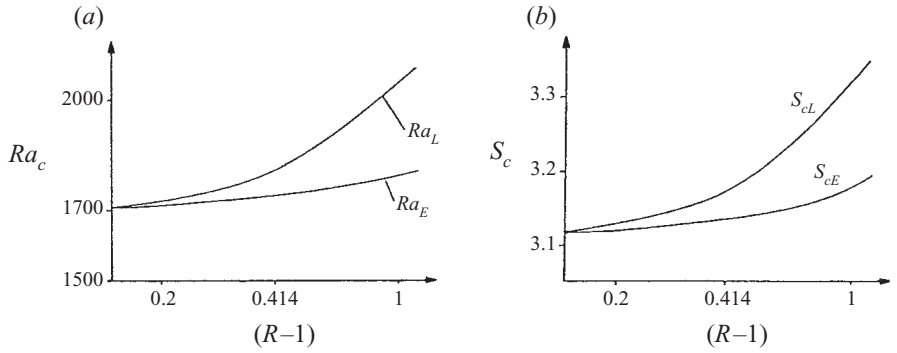

FIGURE 2. Comparison between results from the linear theory and the energy method: (*a*) critical Rayleigh numbers; (*b*) critical wavenumbers.

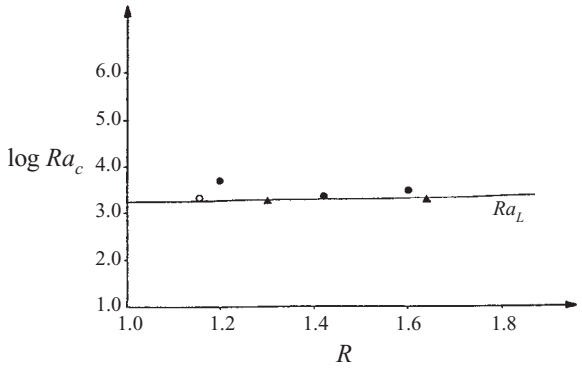

FIGURE 3. Comparison between critical Rayleigh numbers obtained by the linear theory and those obtained experimentally by other authors: ▲, Grigull & Hauf; ○, Liu *et al.*; ●, Powe *et al.*

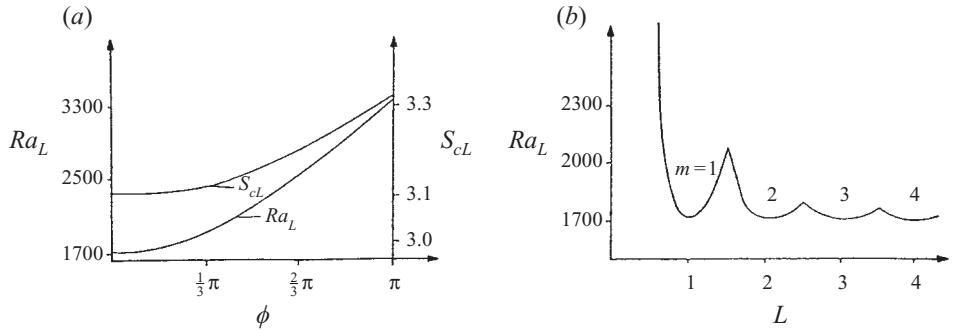

FIGURE 4. Variation of the critical Rayleigh number Ra_L and wavenumber S_{cL} for $R = 1.2$: (*a*) Ra_L and S_{cL} as a function of ϕ; (*b*) Ra_L as a function of L.

The numerical calculation based on setting the corresponding determinant to zero is carried out with an arbitrarily chosen wavenumber and a value of the radius ratio R for which the critical conditions appear. By varying s and calculating the corresponding Ra_r, the values of the linear critical Rayleigh number Ra_L and the linear critical number S_{cL} are calculated. In table 1 and figures 2–4, Ra_L and S_{cL} are based on the annular

thickness. In figures 2(*a*) and 2(*b*), the values of Ra_L and S_{cL} obtained by the numerical model are plotted as a function of $(R-1)$. When R tends to unity, i.e. when the upper part of the annulus approaches a horizontal plane, Ra_L tends to 1708 and S_{cL} to 3.12. This result corresponds to the onset of convection in a horizontal fluid layer and represents a classical result. Figure 3 shows the variation of Ra_L with R and experimental values of Ra_c obtained by various authors with air as the working fluid. In general, the agreement is very good considering there is scatter in the previous results owing to difficulty in the experimental determination of the point of transition. The comparison is restricted to $R \leqslant 2$. Above this value, the consideration of only axisymmetrical perturbations for $\phi = 0$ does not lead to realistic conclusions. Introducing V_r, V_ϕ, and Θ and their partial derivates, the preceding calculation is repeated near $\phi = \frac{1}{24}\pi$. The value of Ra_L obtained for $\phi = \frac{1}{24}\pi$ is then slightly higher than the one found for $\phi = 0$ ($Ra_L = 1804.45$ instead of 1804.21 for $R = 2^{1/2}$).

3.2. *Linear stability for any value of* ϕ

Here a finite volume Q of the cell defined by two concentric cylinders and by two cross-sections at a distance l from one another (figure 1) is considered. These two fictitious cross-sections are assumed to be adiabatic. The boundary conditions are

$$\boldsymbol{v} = \theta = 0 \quad \text{at } r = 1, R \quad \forall \phi \in [0, 2\pi], \quad \forall z \in [0, L], \quad \forall t, \tag{35}$$

$$v_z = \frac{\partial \theta}{\partial z} = 0 \quad \text{at } z = 0, L \quad \forall r \in [1, R], \quad \forall \phi \in [0, 2\pi], \quad \forall t. \tag{36}$$

The formulation of the Galerkin method is applied by inserting θ and $\boldsymbol{v}$ as follows:

$$\theta = \sum_{k=1}^{N} a_k(t)\, \theta_k(r, \phi, z), \quad \boldsymbol{v} = \sum_{k=1}^{N} b_k(t)\, \boldsymbol{v}_k(r, \phi, z). \tag{37}$$

By multiplying the perturbed momentum equation by $\boldsymbol{v}_l$ and the perturbed energy equation by θ_l and integrating each of these two equations over the volume Q, we obtain, using the perturbed continuity equation and Green's theorem

$$\left\langle \frac{\partial \boldsymbol{v}}{\partial t} \boldsymbol{v}_l \right\rangle + \langle (\boldsymbol{v} \cdot \boldsymbol{\nabla} \boldsymbol{V} + \boldsymbol{V} \cdot \boldsymbol{\nabla} \boldsymbol{v}) \boldsymbol{v}_l \rangle = -Pr \langle \boldsymbol{\nabla} \boldsymbol{v} : \boldsymbol{\nabla} \boldsymbol{v}_l \rangle + Pr\, Ra_r \langle \theta \boldsymbol{k} \cdot \boldsymbol{v}_l \rangle, \tag{38}$$

$$\left\langle \frac{\partial \theta}{\partial t} \theta_l \right\rangle + \langle (\boldsymbol{v} \cdot \boldsymbol{\nabla} \Theta)\, \theta_l + (\boldsymbol{V} \cdot \boldsymbol{\nabla} \theta)\, \theta_l \rangle = -\langle \boldsymbol{\nabla} \theta \cdot \boldsymbol{\nabla} \theta_l \rangle, \tag{39}$$

where

$$\langle f(r, \phi, z, t) \rangle = \int_0^L \int_0^{2\pi} \int_1^R \langle f(r, \phi, z, t) \rangle\, r\, \mathrm{d}r\, \mathrm{d}\phi\, \mathrm{d}z,$$

$$\boldsymbol{k} = \cos \phi \boldsymbol{e}_1 - \sin \phi \boldsymbol{e}_2.$$

By replacing θ and $\boldsymbol{v}$ by the values defined in equation (37) and considering the marginal state corresponding to $\mathrm{d}a_k/\mathrm{d}t = \mathrm{d}b_k/\mathrm{d}t = 0$, where $k \in [1, N]$, the following equations are obtained

$$\sum_{k=1}^{N} a_k \langle (\boldsymbol{V} \cdot \boldsymbol{\nabla} \theta_k)\, \theta_l + (\boldsymbol{\nabla} \theta_k \cdot \boldsymbol{\nabla} \theta_l) \rangle + b_k \langle \boldsymbol{v}_k \cdot \boldsymbol{\nabla} \Theta \theta_l \rangle = 0, \tag{40}$$

$$\sum_{k=1}^{N} Pr\, Ra_r\, a_k \langle \boldsymbol{k} \cdot \boldsymbol{v}_l\, \theta_k \rangle - b_k \langle Pr\, (\boldsymbol{\nabla} \boldsymbol{v}_k : \boldsymbol{\nabla} \boldsymbol{v}_l) + (\boldsymbol{v}_k \cdot \boldsymbol{\nabla} \boldsymbol{V} + \boldsymbol{V} \cdot \boldsymbol{\nabla} \boldsymbol{v}_k)\, \boldsymbol{v}_l \rangle = 0. \tag{41}$$

In these calculations, the perturbations $v_r(r, \phi, z)$, $v_z(r, \phi, z)$, and $\theta(r, \phi, z)$ are defined by

$$v_{rk} = f_k(r)\cos(k\phi)\cos(sz)/r, \tag{42}$$

$$v_{zk} = -\mathrm{D}[f_k(r)]\cos(k\phi)\sin(sz)/r, \tag{43}$$

$$\theta_k = h_k(r)\cos(k\phi)\cos(sz), \tag{44}$$

where the functions in r are similar to the trial functions used previously. Moreover, instead of integrating directly between 0 and 2π, integrations are carried out between 0 and ϕ. After a formal calculation of the various integrals, it is noted that near $\phi = 0$ the homogeneous linear algebraic system of equations (40) and (41) is independent of ϕ (ϕ can be factored out of the system when only the first term in the development of the sine and cosine functions is considered). These results show that near $\phi = 0$ the critical Rayleigh number and wavenumber vary slightly. The variations of Ra_L and S_{cL}, as a function of ϕ varying between 0 and 2π, are also determined. The corresponding curves are plotted in figure 4(a) for $R = 1.2$. The calculation is carried out for $R = 1.2$ using the perturbation method. The results show a good approximation of the basic flow only for small R and Rayleigh number. This method permits us to calculate easily the various integrals including the characteristic quantities of the basic flow. Thus, the assumption that the flow stability can only be investigated at the top of the annular layer is justified. Furthermore, when the flow is studied in the whole annular layer, Ra_L is approximately double that of the critical Rayleigh number obtained for $\phi = 0$ (figure 4(a)). Figure 4(b) illustrates the variation of the critical Rayleigh number as a function of L for $R = 1.2$ and for a number of cells chosen such that the Rayleigh number is a minimum.

4. Energy method

For the considered geometry, the basic flow is taken to be a function of r and ϕ and subcritical instabilities are taken into consideration. When the temperature gradient and gravity vary in the same direction, the energy method and the linear theory coincide and the principle of stability exchange is verified. Here, the energy method is applied in order to study the stability of basic flow previously defined by the perturbation method and by the numerical model.

Starting with the perturbed governing momentum and energy equations but not neglecting the second-order terms, multiplying the momentum equation by $\boldsymbol{v}$ and the energy equation by θ, integrating each term of these equations over the whole volume filled by the fluid, and using Green's theorem and the perturbed continuity equation results in

$$\frac{1}{2}\frac{\mathrm{d}}{\mathrm{d}t}\langle \boldsymbol{v}^2\rangle + \langle \boldsymbol{v}\cdot\boldsymbol{L}(V)\,\boldsymbol{v}\rangle = \langle -Pr|\boldsymbol{\nabla v}|^2 + Pr\,Ra_r\,\boldsymbol{k}\cdot\boldsymbol{v}\theta\rangle, \tag{45}$$

$$\frac{1}{2}\frac{\mathrm{d}}{\mathrm{d}t}\langle \theta^2\rangle + \langle \boldsymbol{v}\cdot\boldsymbol{\nabla}\Theta\theta\rangle = -\langle|\boldsymbol{\nabla}\theta|^2\rangle, \tag{46}$$

where

$$\boldsymbol{L}(V) = \tfrac{1}{2}[\boldsymbol{\nabla}V + (\boldsymbol{\nabla}V)^{\mathrm{T}}].$$

Combining equations (45) and (46) and setting $\Phi = (\lambda Ra_r)^{1/2}\theta$ gives the energy equation

$$\frac{1}{2}\frac{\mathrm{d}}{\mathrm{d}t}\langle \boldsymbol{v}^2 + \Phi^2\rangle = -\langle Pr|\boldsymbol{\nabla v}|^2 + |\boldsymbol{\nabla}\Phi|^2\rangle$$
$$- Ra_r^{1/2}\langle(\lambda^{1/2}\boldsymbol{v}\cdot\boldsymbol{\nabla}\Theta - Pr\lambda^{-1/2}\,\boldsymbol{k}\cdot\boldsymbol{v})\,\Phi + Ra_r^{-1/2}\,\boldsymbol{v}\cdot\boldsymbol{L}(V)\boldsymbol{v}\rangle, \tag{47}$$

where λ is a positive coupling parameter. Now setting

$$H = \langle Pr|\nabla \boldsymbol{v}|^2 + |\nabla \Phi|^2 \rangle = 1, \tag{48}$$

and

$$\rho_\lambda^{-1} = \max\,[-\langle(\lambda^{1/2}\boldsymbol{v}\cdot\nabla\Theta - Pr\lambda^{-1/2}\,\boldsymbol{k}\cdot\boldsymbol{v})\,\Phi + Ra_r^{-1/2}\boldsymbol{v}\cdot\boldsymbol{L}(V)\boldsymbol{v}\rangle], \tag{49}$$

we obtain

$$\frac{\mathrm{d}}{\mathrm{d}t}(E) \leqslant 2(-1 + Ra_r^{1/2}/\rho_\lambda), \tag{50}$$

where $E = \langle \boldsymbol{v}^2 + \Phi^2 \rangle$ is the 'energy' term. For $Ra_r^{1/2} < \rho_\lambda$ the global asymptotic stability of the basic flow is ensured. In this case, we have indeed $\mathrm{d}E/\mathrm{d}t < 0$ and the perturbation energy decreases. The problem of optimization of $\rho_\lambda\,\forall\,\Phi$ and $\boldsymbol{v}\in A$ leads to the following variational problem,

$$\delta\left\langle (\lambda^{1/2}\boldsymbol{v}\cdot\nabla\Theta - Pr\lambda^{-1/2}\,\boldsymbol{k}\cdot\boldsymbol{v})\,\Phi + Ra_r^{-1/2}\boldsymbol{v}\cdot\boldsymbol{L}(V)\,\boldsymbol{v} - \frac{2}{\rho_\lambda}p\nabla\cdot\boldsymbol{v} + \frac{1}{\rho_\lambda}(Pr|\nabla\boldsymbol{v}|^2 + |\nabla\Phi|^2)\right\rangle = 0,$$

where $2p/\rho_\lambda$ is the Lagrange's multiplier for $\nabla\cdot\boldsymbol{v} = 0$ and $1/\rho_\lambda$ relative to the equation $H = 1$. Under these conditions we deduce the Euler–Lagrange's equations for this variational problem, with $Ra_r^{1/2} = \rho_\lambda = R_\lambda$ as

$$\tfrac{1}{2}R_\lambda[(\lambda^{1/2}\,\nabla\Theta - Pr\lambda^{-1/2}\,\boldsymbol{k})\,\Phi] + \boldsymbol{v}\cdot\boldsymbol{L}(V) = -\nabla p + Pr\nabla^2\boldsymbol{v}, \tag{51}$$

$$\tfrac{1}{2}R_\lambda(\lambda^{1/2}\,\nabla\Theta - Pr\lambda^{-1/2}\,\boldsymbol{k})\cdot\boldsymbol{v} = \nabla^2\Phi. \tag{52}$$

To solve this problem we use the hypothesis justified in §3.2 that $\phi = 0$, and again consider axisymmetrical two-dimensional perturbations

$$\boldsymbol{v} = [v_r(r)\,\boldsymbol{e}_1 + v_z(r)\,\boldsymbol{e}_3]\exp(\mathrm{i}sz), \tag{53}$$

$$\Phi = \theta(r)\exp(\mathrm{i}sz). \tag{54}$$

By eliminating ∇p in equation (51) and replacing $\boldsymbol{v}$ and Φ by their values given in equations (53) and (54), respectively, we obtain, taking account of the perturbed continuity equation the following equations:

$$\tfrac{1}{2}R_\lambda\left(\lambda^{1/2}\frac{\partial\Theta}{\partial r} - Pr\lambda^{-1/2}\right)v_r = \mathscr{L}(\theta) + \frac{\theta}{r^2}, \tag{55}$$

$$\begin{aligned}&\tfrac{1}{2}R_\lambda\left[\lambda^{1/2}\left(s^2\,\theta\frac{\partial\Theta}{\partial r} + \frac{1}{r^2}\frac{\partial^2\Theta}{\partial\phi^2}\,\mathrm{D}\theta\right) + Pr\lambda^{-1/2}\left(\frac{\mathrm{D}\theta}{r} - s^2\theta\right)\right]\\ &+\frac{1}{2r^2}\frac{\partial}{\partial r}\left[rv_r\left(\frac{1}{r}\frac{\partial^2 V_r}{\partial\phi^2} + \frac{\partial^2 V_\phi}{\partial r\,\partial\phi} - \frac{1}{r}\frac{\partial V_\phi}{\partial\phi}\right)\right] + s^2 v_r\frac{\partial V_r}{\partial r} - \frac{v_r}{r^2}\frac{\partial^3 V_r}{\partial r\,\partial\phi^2} + Pr\,\mathscr{L}^2(v_r) = 0,\end{aligned} \tag{56}$$

where $\mathscr{L}$, $\mathscr{L}^2$, and D are operators defined in §3. The Galerkin method described in §3 gives

$$\sum_{k=1}^{N} a_k\left\langle\theta_l\left(\mathscr{L}(\theta_k) + \frac{\theta_k}{r^2}\right)\right\rangle - b_k\left\langle\tfrac{1}{2}R_\lambda\left(\lambda^{1/2}\frac{\partial\Theta}{\partial r} - Pr\lambda^{-1/2}\right)v_{rk}\,\theta_l\right\rangle = 0, \tag{57}$$

$$\begin{aligned}&\sum_{k=1}^{N} a_k\,\tfrac{1}{2}R_\lambda\left\langle\lambda^{1/2}\left(s^2\,\theta_k\frac{\partial\Theta}{\partial r} + \frac{1}{r^2}\frac{\partial^2\Theta}{\partial\phi^2}\,\mathrm{D}\theta_k\right)v_{rl} + Pr\lambda^{-1/2}\left(\frac{\mathrm{D}\theta_k}{r} - s^2\,\theta_k\right)v_{rl}\right\rangle\\ &+ b_k\left\langle\left(\frac{v_{rl}}{r^3} - \frac{\mathrm{D}v_{rl}}{2r^2}\right)\left[v_{rk}\left(\frac{\partial^2 V_r}{\partial\phi^2} + r\frac{\partial^2 V_\phi}{\partial r\,\partial\phi} - \frac{\partial V_\phi}{\partial\phi}\right)\right]\right.\\ &\left.+ v_{rk}\,v_{rl}\left(s^2\frac{\partial V_r}{\partial r} - \frac{1}{r^2}\frac{\partial^3 V_r}{\partial r\,\partial\phi^2}\right) + Pr\,v_{rl}\,\mathscr{L}^2(v_{rk})\right\rangle = 0.\end{aligned} \tag{58}$$

This leads to the condition for the global flow stability

$$F(R_\lambda, s^2, \lambda^{1/2}) = 0. \tag{59}$$

For a given radius ratio R, a critical Rayleigh number exists for which the global stability is ensured. This number is defined by

$$Ra_E = \min_s(\max_\lambda R_\lambda). \tag{60}$$

Equations (57) and (58) establish the curve of global stability and the critical values Ra_E and S_{cE} for each value of R and several degrees of approximation (table 1). In figures 2(a) and 2(b) Ra_L and S_{cL} are found to tend respectively to 1708 and 3.12 as R approaches unity, i.e. as the layer approaches a plane layer. Moreover, the $Ra_L(R)$ curve always lies above the $Ra_E(R)$ curve and the $S_{cL}(R)$ curve always above the $S_{cE}(R)$ one.

The study of the nonlinear stability based on the energy method gives us a necessary criteria for the global stability of a flow due to natural convection in an annular fluid layer. We thus have found two critical Rayleigh numbers. At $Ra < Ra_E$ the basic flow is globally stable for any perturbation regardless of the amplitude. For $Ra > Ra_L$ the two-dimensional flow is unstable. For $Ra_E < Ra < Ra_L$, the two-dimensional flow is stable for infinitely small perturbations but it may be unstable for perturbations of a given amplitude. As Ra increases to Ra_L, the amplitude of the perturbations able to destabilize the flow approaches zero. For this reason the experimental determination of Ra_L is difficult and some differences are observed between our theoretical results on determination of Ra_L and other experimental results.

5. Numerical results and discussion

The effect on the flow field and thermal structure of varying Rayleigh number is presented for cases of moderate- and large-gap annuli with air as the fluid medium. For the moderate-gap case, comparisons between results of the stability study and numerical analysis are made and factors influencing the size and number of vortical cells which arise owing to thermal instability are investigated. Prandtl number effects are also investigated by analysing a large-gap annulus containing a large Prandtl number fluid. All of the numerical simulations were performed over the entire length of the annulus. Symmetry of the results relative to the annulus mid-axial plane was demonstrated for each case that was studied. In the following discussion of results and in all of the figures, Ra refers to the Rayleigh number based on thickness of the annular layer.

The classification of the annulus geometry considered in the present study as either moderate gap or large gap, depending on the radius ratio R, is based on the flow map of Powe, Carley & Bishop (1969) for air. Their experiments and compilation of experimental results from other investigators indicate that flow in large-gap annuli ($R > 1.71$) remains stable up to much higher Rayleigh numbers than in moderate gap annuli ($1.24 < R < 1.71$). In the present numerical studies, the annulus radius ratios were selected to permit comparison of the numerical solutions with experimental results. The value of $R = 1.6$ employed in the moderate gap numerical study was also used in the experiments by Powe *et al.* (1969). The radius ratio $R = 2.2$ was chosen for investigation of a large-gap annulus since it is close to the values $R = 2.18$ and $R = 2.3$ at which benchmark comparisons of the numerical solutions and experimental results are made. For the case of a large-gap annulus containing a large Prandtl number fluid, the numerical simulations and experiments were both conducted using

$R = 2.1$. Results of the comparisons are provided in §5.2 for moderate-gap annuli and in §6 for large-gap annuli.

Temperature distributions are presented as isotherms at selected axial planes and the upper angular symmetry plane. Flow patterns at the mid-axial plane and the upper angular symmetry plane are presented in terms of streamlines since the normal velocity and the normal gradients of the tangential velocity components are zero at these planes owing to flow symmetry. The z-component of vector potential corresponds to the two-dimensional stream function at the mid-axial plane and the ϕ component of vector potential corresponds to the two-dimensional stream function at the angular symmetry plane. Inner and outer cylinder heat transfer results are presented as three-dimensional surface plots of local Nusselt number. To be consistent with previous studies, the results here are all presented in terms of r_o non-dimensionalization.

To ensure the numerical results were not dependent on grid size, a mesh refinement procedure was adopted in which results for different grid distributions were compared. In this procedure, the number of grid points in the radial direction was first successively increased while the angular and axial grid points were held constant. Keeping the number of axial grid points the same, the number of angular grid points was then successively increased using the grid size in the radial direction obtained from the previous step. With the angular and radial grid sizes thus established, the number of grids in the axial direction was then successively increased. Finally, the number of grids in all three directions were increased to determine the grid size which yielded grid independent results. The grid refinement procedure was conducted for each of the cases studied. Using this procedure, it was determined that up to 31, 61, and 225 grid points were required in the radial, angular, and axial directions, respectively, to achieve grid independence.

Sufficiently small timesteps in the range of 10^{-6} to 10^{-3} were used to obtain timestep-independent solutions. In separate numerical runs, the timestep was initially set to a large value and then progressively decreased until the transient solution no longer changed. In this manner, the step size which yielded timestep-independent results was determined for each case studied.

5.1. *Large-gap annulus with air*

Numerical simulations were conducted for annuli having a radius ratio of $R = 2.2$, which falls in the large-gap category. The Rayleigh number was successively increased from 10^2 to 10^4, which enabled the evolution of steady state three-dimensional flow structures to be analysed. The results presented in this section are for an annulus of dimensionless length $L = 10$, in which temperatures at the mid-axial region are shown to correspond closely to those associated with two-dimensional flow. In §5.2, the results are compared to those for a moderate-gap annulus and similarities and differences in the flow fields and temperature distributions are presented.

At the lowest Rayleigh number studied of 100, crescent-shaped flow patterns centred on $\phi = \pm\frac{1}{2}\pi$ are present in the axial planes of the annulus. The velocity of the recirculating flow is very small and does not affect the shape of the isotherms, which are concentric circles in all of the axial planes indicating heat transfer occurs essentially by conduction only. The effect of the endwalls on the isotherms is not discernible. As the Rayleigh number is increased to 10^3, the influence of the flow on the temperature field within the annulus becomes more noticeable. This is seen in figure 5(*a*), where the isotherms and streamlines at the mid-axial plane are plotted on the right- and left-hand sides, respectively. The isotherms take on the appearance of eccentric circles, and the centre of flow rotation is shifted slightly upward from $\phi = -\frac{1}{2}\pi$. Heat transfer still

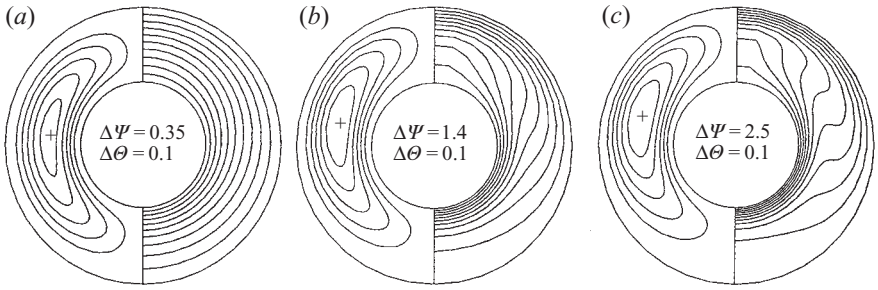

FIGURE 5. Effect of Ra on convection at the mid-axial plane for $R = 2.2$, $L = 10$, $Pr = 0.7$ with streamlines on the left and isotherms on the right: (*a*) $Ra = 10^3$; (*b*) $Ra = 4 \times 10^3$; (*c*) $Ra = 10^4$.

occurs mostly by conduction, as evidenced by the calculated steady state mean Nusselt number at the mid-axial plane of 1.042. For $Ra = 10^3$, the isotherms do not vary with respect to axial position within the range $\frac{1}{8}L < z < \frac{7}{8}L$. At $z = 0$ and $z = L$, the isotherms are more evenly spaced between the inner and outer cylinders near $\phi = 0$ as compared to the other axial locations.

With further increase in Rayleigh number to 4×10^3, the effects seen at lower Rayleigh number are significantly amplified owing to the increased strength of the flow as shown in figure 5(*b*). The centre of rotation of the flow has shifted upward compared to $Ra = 10^3$ and the isotherms are now distorted and grouped more closely against the bottom of the inner cylinder and top of the outer cylinder, where the inner and outer cylinder thermal boundary layers are respectively thinnest. The overall heat transfer has departed significantly from that of conduction, with the mean Nusselt number at the mid-axial plane increasing to 1.486. The influence of the endwalls becomes more pronounced and extends further into the annulus. The core region in which temperatures are essentially independent of axial position now extends from roughly $z = \frac{1}{4}L$ to $z = \frac{3}{4}L$.

For an even higher Rayleigh number of 10^4, the shape of the isotherms at the mid-axial plane presented in figure 5(*c*) clearly shows the highest extraction of heat from the lower portion of the inner cylinder, upward flow of heated fluid from the top of the inner cylinder, and locally increased heating of the top of the outer cylinder by the buoyant fluid. The subsequent reduction in fluid temperature as the flow moves downward along the outer cylinder surface is apparent. The isotherms are inverted indicating that separation of the inner and outer cylinder thermal boundary layers has occurred, which is due to the strong recirculation of the flow field. The overall heat transfer has increased to almost twice that of conduction, with a mean Nusselt number at the mid-axial plane of 1.965. The trend of increased height of the centre of flow rotation with higher Rayleigh number is seen by comparison of figures 5(*a*), 5(*b*), and 5(*c*). Three-dimensional effects become more prominent and of greater axial extent for Rayleigh number of 10^4. The isotherms are now substantially distorted in the top of the annulus at $z = 0$ and the core region encompasses a smaller zone extending from approximately $z = \frac{3}{8}L$ to $z = \frac{5}{8}L$.

To better illustrate the flow mechanisms responsible for the significant change in the temperature field near the endwalls with increasing Rayleigh number, which is most prominent at the uppermost angular position, streamlines and isotherms in the upper angular symmetry plane are plotted in figures 6(*a*) and 6(*b*), respectively. For $Ra = 10^3$, it is seen in figure 6(*a*) that a rotational cell is present next to each endwall in the upper region of the annulus. The cells rotate clockwise on the right-hand end of the annulus and counterclockwise on the left as indicated. The strength of the cells is very

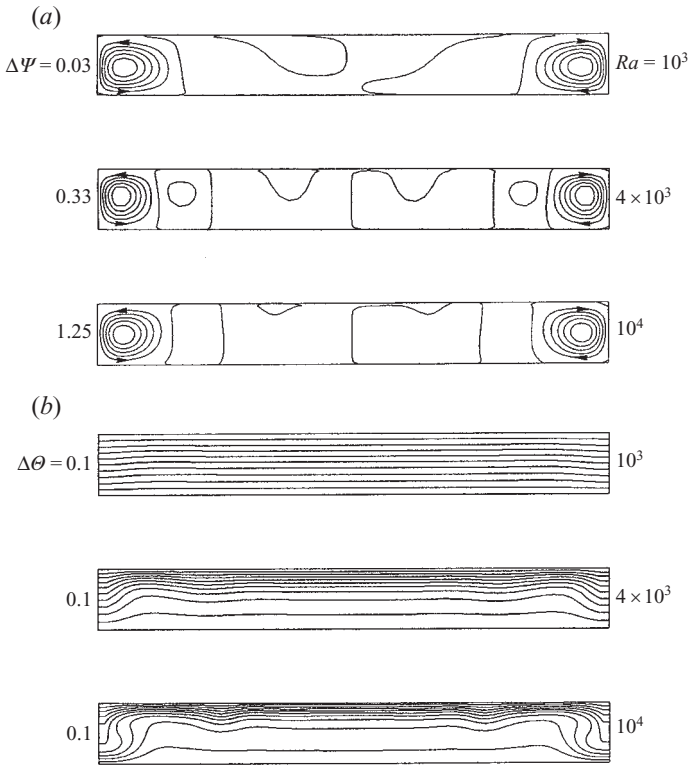

FIGURE 6. Effect of Ra on convection at the upper angular symmetry plane for a large gap annulus for $R = 2.2$, $L = 10$, $Pr = 0.7$: (a) streamlines; (b) isotherms.

weak at this Rayleigh number which results in only slight distortion of the isotherms in the vicinity of the endwalls, as seen in figure 6(b). The maximum value of the dimensionless stream function associated with the cells is 0.17. Between the two cells, axial velocities of the flow are very small compared to radial velocities and circulation in the (r, z)-plane is not appreciable. As a result, the isotherms are seen as horizontal lines.

When the Rayleigh number is increased to 4×10^3, the end cells gain considerable strength with the maximum value of the stream function increasing to 2.01. Owing to increased viscous shear forces, a weak counter-rotating secondary flow pattern is produced next to each end cell, as seen in figure 6(a). The isotherms clearly reflect the presence of the rotating cell and secondary pattern at each end of the annulus, as seen in figure 6(b). Between the secondary patterns, only very weak (r, z)-plane circulation is present. Within the core region of the annulus, the isotherms appear as approximately horizontal lines.

At the highest Rayleigh number of 10^4, the maximum value of the stream function associated with the end cells has increased to 7.52 and the size of the cells has grown, as seen in figure 6(a). Accordingly, their influence on the isotherms has moved further toward the centre of the annulus which reduces the size of the core region to $\frac{3}{8}L < z < \frac{5}{8}L$ as previously mentioned. Owing to the greater rotational strength of the cells, the isotherms in the end regions are now inverted and the depression in isotherms associated with each secondary pattern is larger than for $Ra = 4 \times 10^3$, as seen in figure 6(b). As in this lower Rayleigh number case, between the secondary patterns the flow remains stable and only very weak circulation occurs in the (r, z)-plane.

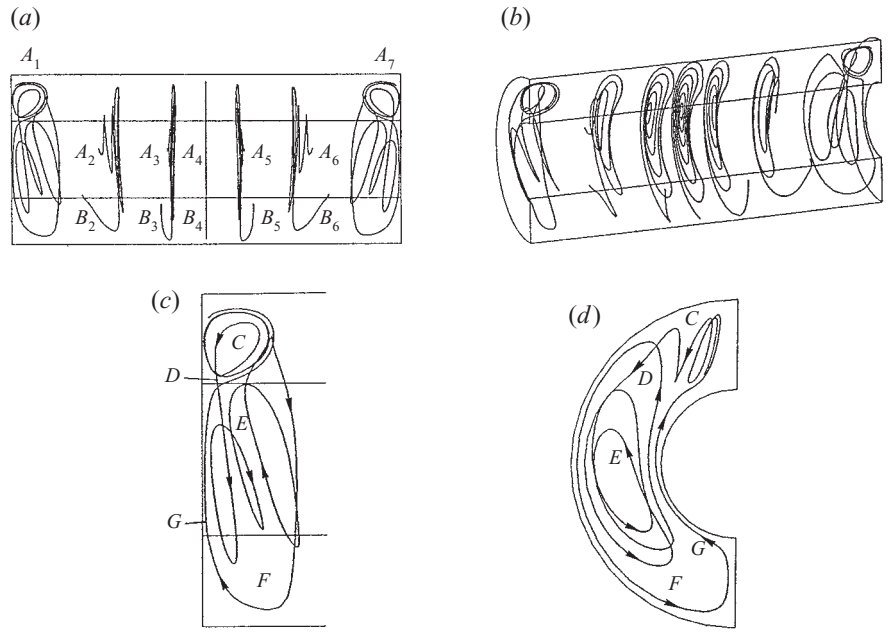

FIGURE 7. Fluid particle paths in a large gap annulus for $Ra = 10^4$, $R = 2.2$, $L = 10$, $Pr = 0.7$: (*a*) side view; (*b*) perspective view; (*c*) side view of end cell region; (*d*) end view of end cell region.

Fluid particle path plots for $Ra = 10^4$ are presented in figure 7 to provide additional insight into the flow structure. The pathlines seen in figures 7(*a*) and 7(*b*) represent the trajectories of seven massless particles injected into the flow field. In order to illustrate the flow-field characteristics over the length of the annulus, a single particle is released into each of the rotating end cells in the upper part of the annulus (A_1 and A_7) and the remaining five particles are released at axial positions of $z = 0.22L$ (A_2), $0.4L$ (A_3), $0.5L$ (A_4), $0.6L$ (A_5), and $0.78L$ (A_6) near the centre of rotation of the primary flow. The paths of the five particles released between the endwall regions reflect the two-dimensional nature of the flow near the mid-axial plane and the departure from two-dimensional flow outside the core region. The symmetry of flow about the mid-axial plane is seen in the movement of the particle released at $z = 0.5L$ (A_4), which traces a series of increasingly larger crescent-shaped patterns with no axial movement. As particles are released at positions further from the mid-axial plane, the component of axial velocity increases, as seen by the further axial progression of particles introduced at $z = 0.22L$ and $0.78L$ compared to $0.4L$ and $0.6L$, respectively (A_2 versus A_3 and A_6 versus A_5). These particles trace a series of increasingly larger crescent patterns as they slowly proceed axially inward. Upon reaching the bottom part of the annulus near the outer cylinder, the particles reverse axial direction and begin to move in the direction of the endwalls within the lower region of the annulus (locations B_2, B_3, B_5, B_6). This indicates that a relatively low-speed secondary global circulation occurs on each side of the mid-axial plane, with flow closer to the centre of rotation of the main flow moving toward the mid-axial plane and flow in the lower part of the annulus that is close to the outer cylinder wall moving in the opposite direction.

Enlarged views of the particle path associated with the left-hand end cell region, which is the reflection of that in the right-hand end cell region owing to symmetry about the mid-axial plane, are provided in figures 7(*c*) and 7(*d*). After release of the

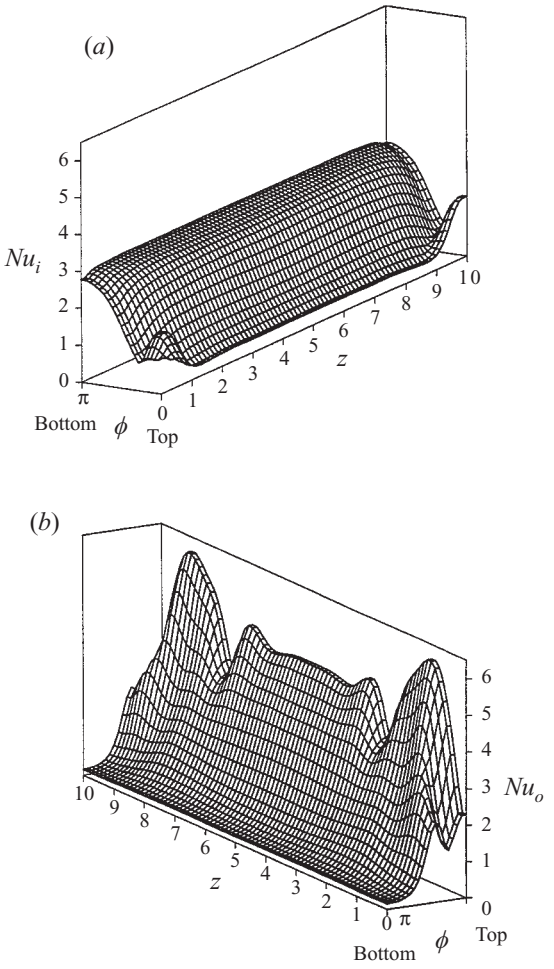

FIGURE 8. Local Nusselt number distribution for $Ra = 10^4$, $R = 2.2$, $L = 10$, $Pr = 0.7$: (*a*) inner cylinder; (*b*) outer cylinder.

particle into the end cell, it is seen to follow an angled spiral path (location C) in the direction transverse to the angular symmetry plane. At approximately $\phi = -\frac{1}{4}\pi$, the particle becomes entrained in the main annulus flow (location D) and subsequently traces a series of crescent patterns (region E) as it moves axially away from the endwall. Upon reaching the axial extent of the end cell region, it reverses direction and proceeds back toward the endwall in a larger crescent that surrounds the previous smaller ones. After reaching the lower part of the annulus (location F), it rises along the inner cylinder surface (starting at location G) and re-enters the rotating end cell at the top at approximately the same position as its release point, thereby closing a three-dimensional circuit.

A plot of the local Nusselt number distribution on the inner and outer cylinders is given in figures 8(*a*) and 8(*b*), respectively, for $Ra = 10^4$. As seen in figure 8(*a*), the inner cylinder Nusselt number shows little variation in the axial direction over most of the annulus. The inner cylinder Nusselt number is highest at the bottom ($\phi = \pi$) where the associated thermal boundary layer is thinnest. As the fluid rises along the hot inner cylinder surface the boundary-layer thickness increases and the Nusselt number

decreases, reaching a minimum value at the top of the cylinder ($\phi = 0$) except near $z = 0$ and $z = L$. At these locations, there are localized peaks owing to the presence of the end vortices in the annulus, which transport fluid cooled by the outer cylinder surface directly to the inner cylinder surface resulting in locally increased heat flux from the inner cylinder. In the lower regions of the annulus ($\phi > \frac{1}{3}\pi$), there is a localized reduction in the inner cylinder Nusselt number at $z = 0$ and $z = L$ owing to the endwalls which retard the adjacent flow.

The outer cylinder Nusselt number shown in figure 8(*b*) exhibits the opposite trend of decreasing magnitude with increased angular position. This occurs since the outer cylinder thermal boundary layer is thinnest at the top of the annulus and increases in thickness as the flow proceeds downward, with the outer cylinder Nusselt number reaching a minimum at the bottom of the annulus. The end vortices at the top are seen to have a profound effect on the local heat transfer, with large peak outer cylinder Nusselt numbers occurring at $\phi = 0$ where heated fluid entrained in the vortices impinges on the outer cylinder at relatively high velocity. At $z = 0$ and $z = L$, the fluid entrained in the vortices leaves the outer cylinder surface resulting in local minima. The effects of the circulation adjacent to the end vortices (see figure 6(*a*)) are seen as local reductions in the outer cylinder Nusselt number near $\phi = 0$ where the fluid moves away from the outer cylinder toward the inner cylinder. The outer cylinder Nusselt number is seen to be essentially independent of axial position over a reduced central core region covering approximately $\frac{1}{8}$ of the axial length.

From the numerical results, it is concluded that at higher Rayleigh numbers which precede transition to oscillatory flow (which was observed to occur at $Ra = 6.6 \times 10^4$ in the present experimental study) the steady flow field in a sufficiently long closed annulus of $R = 2.2$ is comprised of several distinct regions, each of which is symmetric about the mid-axial plane. In the core region of the annulus, the axial velocities are very small and the temperature distribution corresponds to that of two-dimensional flow. Adjacent to each endwall, a region exists in which a complex three-dimensional recirculating flow consisting of a transverse vortex in the upper portion of the annulus and a double helical flow structure in the lower part occurs. Here, the buoyant upward flow is retarded owing to the viscous shearing effect of the walls which produces a transverse vortical cell. Fluid rising along the inner cylinder becomes entrained in this cell and is transported along a spiral path back to the primary flow. It then traces an inner crescent-shaped helix away from the endwall followed by an outer helical loop back toward the wall before re-entering the vortex. Between the end region and the core region, a third region is present in which the primary flow circulation occurs in the (r, ϕ)-plane and a much lower speed axial movement is also present. Within this region, there is noticeable displacement of the isotherms in the upper part of the annulus owing to lower-strength circulation next to the end cell region.

5.2. *Moderate-gap annulus with air*

Three-dimensional buoyancy-driven flow and heat transfer within concentric horizontal cylinders having a radius ratio of $R = 1.6$ were investigated numerically for air ($Pr = 0.7$). The simulations were performed over a range of Rayleigh numbers between 10^2 and 4.5×10^3, which permitted investigation of stable flow structures occurring at lower Rayleigh numbers and post-transitional flow structures which arise at Rayleigh numbers exceeding the critical value for instability. The investigation was conducted for an annulus with dimensionless length $L = 4$. To illustrate the effects of annulus length on the secondary flow and associated temperature fields, results are also presented for $L = 4.5$, 5, and 5.5.

Similar to the large-gap annulus case, at Rayleigh number of 100 symmetric crescent-shaped flow patterns centred on $\phi = \pm\frac{1}{2}\pi$ are present in the axial planes of the moderate gap annulus and the isotherms at each axial plane appear as concentric circles. In each (r, z)-plane, the isotherms are viewed as horizontal lines without any noticeable distortion in the vicinity of the end walls. At Rayleigh number of 10^3, however, the influence of the natural convection flow on the temperature field within the annulus becomes more noticeable. The isotherms at the axial planes within the annulus appear as eccentric circles while at the endwalls they are slightly more evenly spaced between the inner and outer cylinders at $\phi = 0$. In this pseudoconduction regime, heat transfer takes place almost entirely by conduction with a mean Nusselt number at the mid-axial plane of 1.021. Within the range of approximately $\frac{1}{8}L < z < \frac{7}{8}L$, the temperature distribution is invariant with respect to axial position.

The next highest Rayleigh number studied was 2×10^3, which exceeds the linear critical Rayleigh number of $Ra_L = 1.9 \times 10^3$ for $R = 1.6$ determined from the stability analysis. At $Ra = 2 \times 10^3$, the isotherms within the annulus are grouped closer to the bottom of the inner cylinder and the top of the outer cylinder where heat transfer is highest at the inner and outer cylinders, respectively. At the endwalls, the isotherms are nearly evenly spaced between the inner and outer cylinders at $\phi = 0$. The mean Nusselt number at the mid-axial plane has increased to 1.100 indicating the heat transfer has begun to depart from that of purely conduction. In contrast to the lower Rayleigh number results and also the large-gap annulus results presented in § 5.1, the temperature distribution near $\phi = 0$ varies over the entire length of the annulus and there is no longer a distinct core region centred on the mid-axial plane. As shown later, this is an indication of the onset of secondary flows within the annulus owing to instability phenomena. The lack of a core region at $Ra = 2 \times 10^3$ was also established for longer annuli, confirming this is not simply the result of insufficient annulus length.

As the Rayleigh number is increased further to 2.8×10^3 dramatic changes in the temperature field arise which reflect the more complete development of secondary flows resulting from the thermal instabilities. The isotherms are essentially unchanging with respect to axial position at angular positions between approximately $\frac{1}{3}\pi$ and π, and are spaced closer to the bottom of the inner cylinder. However, in the upper part of the annulus there are significant differences in the spacing and shape of isotherms from one axial plane to another.

Plots of streamlines and isotherms in the upper angular symmetry plane, where the greatest changes occur with increased Rayleigh number, are provided in figures 9(*a*) and 9(*b*), respectively. At $Ra = 10^3$, a rotational cell is seen to be present next to each endwall. The cells rotate in opposite directions, clockwise on the right-hand end of the annulus and counterclockwise on the left. Their strength is very low with a maximum value of stream function at the upper angular symmetry plane of 0.12, which produces only a slight distortion of the otherwise horizontal isotherms in the vicinity of the endwalls. As previously mentioned, the core region in which temperatures are independent of axial position lies within approximately $\frac{1}{8}L < z < \frac{7}{8}L$. The axial velocities of the flow are relatively small in the region between the end cells and circulation in the angular symmetry plane is weak there. At this low Rayleigh number, the stable flow patterns and isotherms bear a resemblance to those in a large-gap annulus as seen by comparison between figures 6 and 9 at $Ra = 10^3$.

When the Rayleigh number is increased beyond $Ra_L = 1.9 \times 10^3$ to $Ra = 2 \times 10^3$, the end cells become much stronger, with the maximum value of the stream function at the upper angular symmetry plane increasing to 1.04. The region between the end cells is now filled by two pairs of counter-rotating cells symmetric about the mid-axial plane,

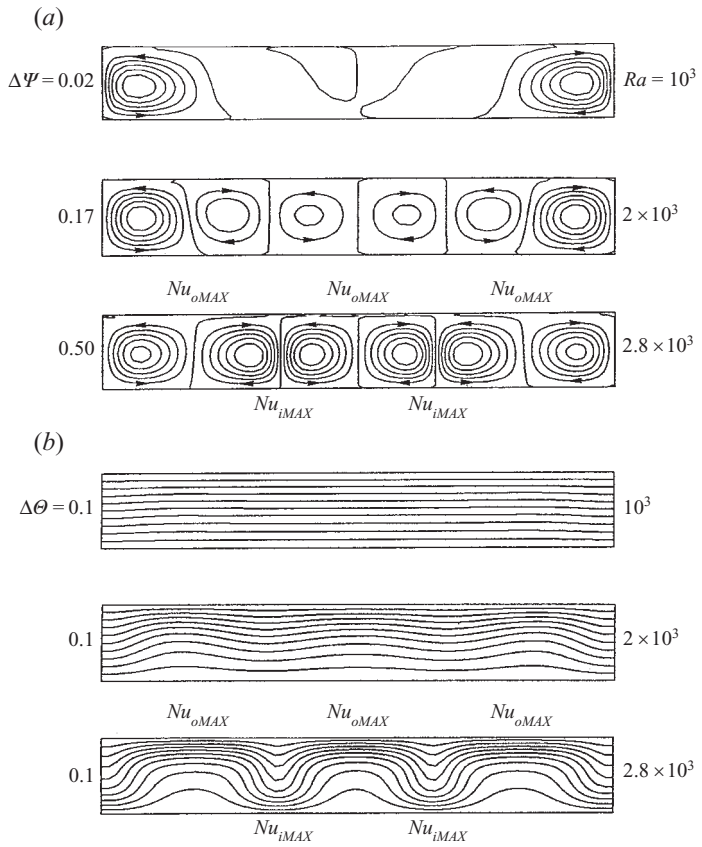

FIGURE 9. Effect of Ra on convection at the upper angular symmetry plane for a moderate gap annulus for $R = 1.6$, $L = 4$, $Pr = 0.7$: (a) streamlines; (b) isotherms.

as seen in figure 9(a). Although the inner cells are weaker than the end cells, they are nonetheless strong enough to markedly influence the temperature distribution. The alternating elevation and depression of the isotherms along the length of the annulus corresponding to the opposing direction of rotation of adjacent cells is seen in figure 9(b). Owing to the presence of the inner cells in the upper portion of the annulus, a core region no longer exists. As seen in figure 9(a), at $Ra = 2 \times 10^3$ the two cells adjacent to the mid-axial plane occupy approximately the same space as the end cells. As the Rayleigh number is increased further, the strength of the inner cells increases faster than that of the end cells and becomes slightly greater prior to reaching $Ra = 2.8 \times 10^3$. The two end cells increase in size and the two innermost cells decrease in size until approximately $Ra = 2.8 \times 10^3$, at which point the cell sizes change relatively little with further increase in Rayleigh number. The value of $Ra \approx 2.8 \times 10^3$ obtained from the present numerical studies, which marks the full transition to three-dimensional secondary flows in the upper portion of the annulus, is in excellent agreement with the transition flow map of Powe *et al.* (1969) derived from experimental results of several investigators.

Streamlines in the upper angular symmetry plane for a Rayleigh number of 2.8×10^3 are shown in figure 9(a). At this Rayleigh number, the maximum value of the stream function at the upper angular symmetry plane is 3.01 and is associated with the inner

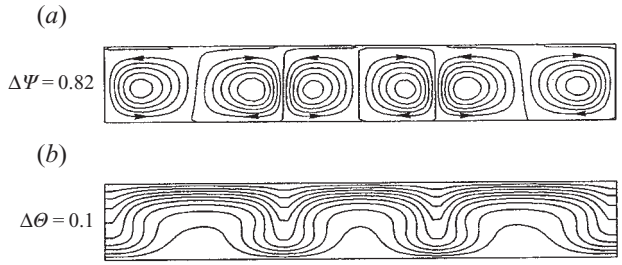

FIGURE 10. Streamlines and isotherms at the upper angular symmetry plane for a moderate gap annulus for $Ra = 4.5 \times 10^3$, $R = 1.6$, $L = 4$, $Pr = 0.7$: (*a*) streamlines; (*b*) isotherms.

cells that arise owing to thermal instability. The end cells which existed previous to transition are slightly weaker than the inner cells owing to the viscous shearing effect of the endwalls. The axial dimension of the two centre cells is smallest and the dimension of the end cells is largest. A comparison of the axial wavenumber based on annular thickness s' with S_{cL}, the critical wavenumber for an infinitely long annulus obtained from the linear stability analysis, can be made using $s' = m\pi(r_o - r_i)/l$ where l is based on the size of cells adjacent to the mid-axial plane (since these are least influenced by the slower rotating end cells). This yields $s' = 3.14$ which compares very well with $S_{cL} = 3.21$. The variation of isotherms in the upper part of the annulus for $Ra = 2.8 \times 10^3$ is shown in figure 9(*b*). The S-shaped appearance of isotherms within each cell owing to the high rotational strength is clearly seen. The spacing of isotherms reflects the direction of cell rotation, with closer spacing at the cylinder surfaces corresponding to where the flow cooled by the outer cylinder and heated by the inner cylinder impinges on the inner and outer cylinders, respectively.

An example of higher Rayleigh number results is presented in figures 10(*a*) and 10(*b*), where plots of the streamlines and temperature distribution, respectively, at the upper angular symmetry plane for $Ra = 4.5 \times 10^3$ are displayed. The maximum value of the stream function associated with the inner cells is 4.91 compared to 3.01 for $Ra = 2.8 \times 10^3$. Comparison of the streamlines in figures 9(*a*) and 10(*a*) shows the tendency of the two innermost vortical cells to become smaller with increased Rayleigh number until, at $Ra = 2.8 \times 10^3$, they approximately attain the natural size predicted by the stability theory for an infinitely long annulus, and then remain essentially constant in size as the Rayleigh number is increased further.

The three-dimensional nature of the flow at high Rayleigh numbers is illustrated by the fluid particle path plots presented in figure 11 for $Ra = 2.8 \times 10^3$. In these plots, a particle is introduced into each of the six rotational cells present at the top of the annulus (locations A_1–A_6). The ensuing pathlines show the primary flow features present in the moderate-gap annulus including similarities and differences between the end cells and inner cells. In figures 11(*a*) and 11(*b*) all six pathlines are shown, whereas in figures 11(*c*) and 11(*d*) views of the end cell region pathlines and the inner cell pair pathlines, respectively, are shown.

As seen in figure 11(*c*), a particle injected into an end cell follows a spirally rotating path transverse to the angular symmetry plane (location C) until becoming entrained in the primary flow at approximately $\phi = -\frac{1}{4}\pi$ (location D). It then proceeds axially inward in an increasingly larger crescent-shaped helical pattern (region E seen in figures 11(*a*) and 11(*c*)) until reaching the axial limit of the end cell region. At this point, it loops over the original spiral path and follows an even larger crescent-shaped route downward along the outer cylinder wall to the bottom of the annulus

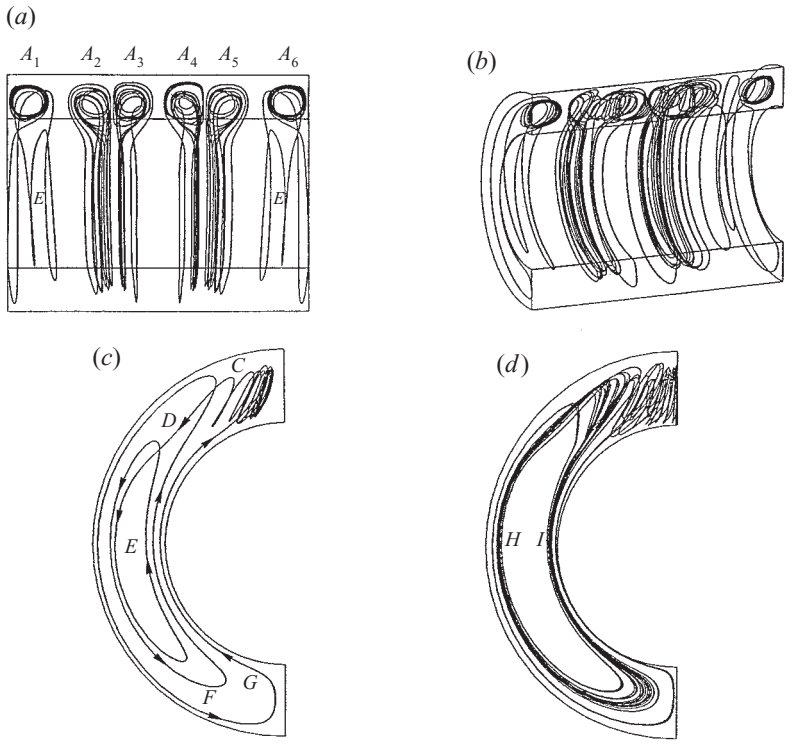

FIGURE 11. Fluid particle paths in a moderate gap annulus for $Ra = 2.8 \times 10^3$, $R = 1.6$, $L = 4$, $Pr = 0.7$: (*a*) side view; (*b*) perspective view; (*c*) end view of end cell region only; (*d*) end view of inner cell pair.

(location *F*) and back up along the inner cylinder surface (starting at location *G*) until it re-enters the spiral vortex at the top of the annulus. The overall movement of particles in the end cells is therefore similar to that in the end cell region of a large-gap annulus shown in figure 7. A particle injected into one of the inner cells of the moderate gap annulus (figure 11(*d*)) follows approximately the same initial spiral trajectory into the primary flow as in the end cell. After this, it proceeds somewhat differently making a single crescent loop with much less change in axial position, first moving downward near the outer cylinder surface (*H*) and then upward adjacent to the surface of the inner cylinder (*I*). Upon reaching the upper part of the annulus it is briefly entrained in the spiral vortex before starting another single crescent circuit in the main flow. The particle continues tracing a number of such circuits within the axial boundaries of that particular cell. The motions described above for particles introduced into the inner cells qualitatively match the sketch of experimental results provided by Grigull & Hauf (1966) for spiral convection in an air filled annulus.

The inner and outer cylinder local Nusselt number distributions are plotted in figures 12(*a*) and 12(*b*), respectively, for $Ra = 2.8 \times 10^3$. Between $\phi = \frac{1}{3}\pi$ and $\phi = \pi$ the inner cylinder Nusselt number is independent of axial position over most of the annulus with a small reduction adjacent to the end walls. Also within this angular range, the basic trend of higher inner cylinder Nusselt number with increasing angular position is consistent with that in a large-gap annulus shown in figure 8(*a*). In the range $\phi = 0$ to $\phi = \frac{1}{3}\pi$, however, there are substantial differences compared to the large-gap results in the region between the end vortices. These are, of course, a result of the inner vortex

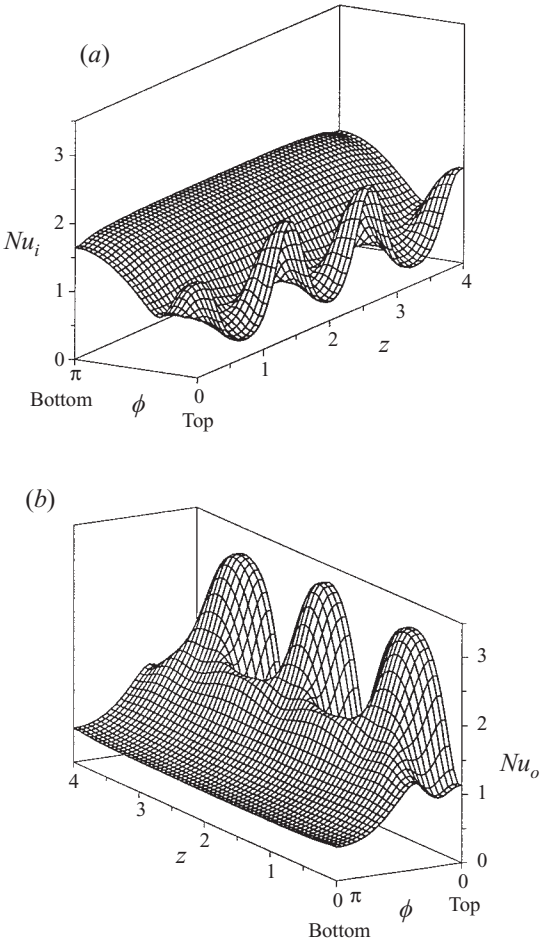

FIGURE 12. Local Nusselt number distribution for $Ra = 2.8 \times 10^3$, $R = 1.6$, $L = 4$, $Pr = 0.7$: (*a*) inner cylinder; (*b*) outer cylinder.

pairs present in the moderate gap annulus which result from instability. As seen in figure 12(*a*), there are two large peaks in inner cylinder Nusselt number corresponding to where fluid entrained in the inner vortex pairs is first cooled by the outer cylinder and then impinges on the inner cylinder (Nu_{iMAX} in figures 9(*a*) and 9(*b*)). Owing to the greater strength of the inner vortex pairs, these are larger than the local peaks at $z = 0$ and $z = L$ associated with the end vortices. The inner cylinder Nusselt number at $\phi = 0$ varies by a factor of 6.45 over the length of the annulus.

As shown in figure 12(*b*), in the lower portion of the annulus the outer cylinder Nusselt number is essentially independent of axial position, becomes smaller with increased angular position, and is a minimum at $\phi = \pi$ which are the same trends seen in the larger-gap annulus results in figure 8(*b*). However, in the upper part of the annulus the moderate gap outer cylinder Nusselt number shows a dramatic variation in the axial direction resulting from the inner vortex pairs. There are three local maxima occurring at $\phi = 0$ which are associated with the flow entrained by the vortices moving upward from the hot inner cylinder and meeting the cool outer cylinder (Nu_{oMAX} in figures 9(*a*) and 9(*b*)). There are also four local minima at $\phi = 0$

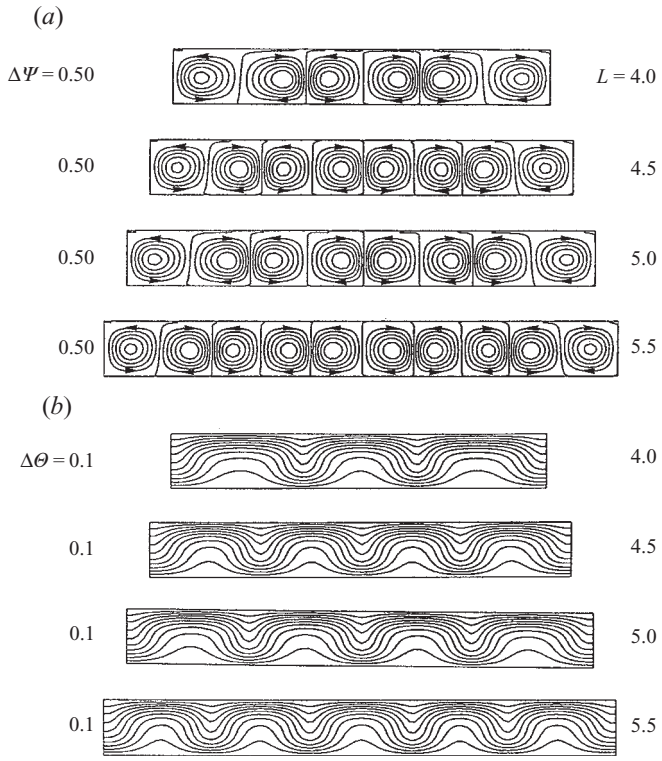

FIGURE 13. Effect of annulus length on convection at the upper angular symmetry plane for $Ra = 2.8 \times 10^3$, $R = 1.6$, $Pr = 0.7$: (*a*) streamlines; (*b*) isotherms.

Annulus length L	Number of cells	Mid-axial cell size (dimensionless)
4	6	0.60
4.5	8	0.53
5	8	0.60
5.5	10	0.55

TABLE 2. Number and size of vortical cells in the annulus

corresponding to the locations of downward movement of fluid away from the outer cylinder, even though the perspective in figure 12(*b*) does not clearly show all four minima. The outer cylinder Nusselt number at $\phi = 0$ varies by a factor of 2.85 over the length of the annulus.

The effect of annulus length on the spiral vortex cells was examined by comparing results at $Ra = 2.8 \times 10^3$ for the cases of $L = 4$, $L = 4.5$, $L = 5$, and $L = 5.5$. A plot of the upper angular symmetry plane streamlines and isotherms for each case is provided in figures 13(*a*) and 13(*b*), respectively. Successively increasing annulus length from $L = 4$ to $L = 5.5$ in increments of $\Delta L = 0.5$ is seen to result in either expansion of the existing cells or the addition of more inner cells, always one counter-rotating cell pair at a time. The cell sizes vary somewhat in order to accommodate an integral number of pairs between the end cells as shown in table 2. The dimensionless mid-axial cell sizes given in table 2 are within $+2\%$ and -10% of the cell size of 0.59 calculated for

an infinitely long annulus, which is obtained from $l = m\pi(r_o - r_i)/S_{cL}$ with $m = 1$. Our results have shown that cell size is dependent not only on the natural size predicted by the stability theory for an infinitely long annulus and the increase in Rayleigh number above the critical value, but also on the length of the annulus with solid endwalls into which an integral number of vortex pairs must fit in the space between end vortices.

The transverse vortices which form in the upper part of the moderate gap annulus behave similarly in some aspects to the natural convection rolls which arise in a three-dimensional rectangular box heated from below. Using a Galerkin procedure, Davis (1967) investigated the linear stability of quiescent fluid in the latter configuration including the influence of the lateral walls. He found that the rolls always form parallel to the shorter walls of the box, and when the gap thickness is less than the other dimensions of the box the rolls are of nearly square cross-section. These results were confirmed experimentally by Stork & Muller (1972). It was found in our studies that, in a manner similar to the three-dimensional box, the transverse vortices in the upper part of the moderate-gap annulus set-up parallel to the endwalls which form the shorter sides of the upper region of the annulus. The cross-section of the vortices is similarly nearly square.

Stork & Muller (1972) observed experimentally that an even or odd number of rolls can form in the rectangular box, but an even number is preferred. In the moderate-gap annulus, however, our numerical results indicate that only an even number of vortical cells form between the cells located at the endwalls. This is believed to be due to the presence of these end cells, which are in place prior to the onset of instabilities. The end cells are driven by the primary natural convective flow in the annulus, and their directions of rotation are opposite to each other. Owing to viscous shearing effects, the end cells determine the directions of rotation of the adjacent vortical cells which form owing to instability. Since all of the cells are counter-rotating, it can be shown that only an even number can fill the space between the opposite rotating end cells. In the rectangular box, there are no pre-existing end rolls and therefore an even number of rolls does not necessarily occur.

From our numerical results, it is seen that changes in the temperature field in the upper portion of the moderate-gap annulus as the Rayleigh number is increased above the critical value for instability are due to the emergence of three-dimensional flows. The flows are comprised of an integral number of transverse vortex pairs located between the annulus end vortices, all of which are symmetric about the mid-axial plane. The end vortices result from the viscous shear imposed by the solid endwalls and are in place prior to the formation of the inner vortex pairs which arise owing to thermal instability. Flow within the end vortex zones follows a closed loop in which fluid inside the vortex is transported spirally in the angular direction into the primary flow and then follows a helical path axially away from the endwall. At the inner axial boundary of the zone the fluid reverses axial direction and moves along a larger helical loop until eventually re-entering the vortex. Within the inner vortex zones, the flow initially proceeds from the vortex into the primary flow in the same spirally rotating manner, but subsequently behaves differently. After completing one crescent circuit within the annulus it becomes briefly entrained in the spiral vortex prior to initiating another single circuit. Within the inner vortex zones the flow is three-dimensional above approximately $\phi = \frac{1}{3}\pi$ and more nearly two-dimensional below this. In the end vortex zone the flow is also three-dimensional above $\phi = \frac{1}{3}\pi$, but below this there is a significant component of axial velocity.

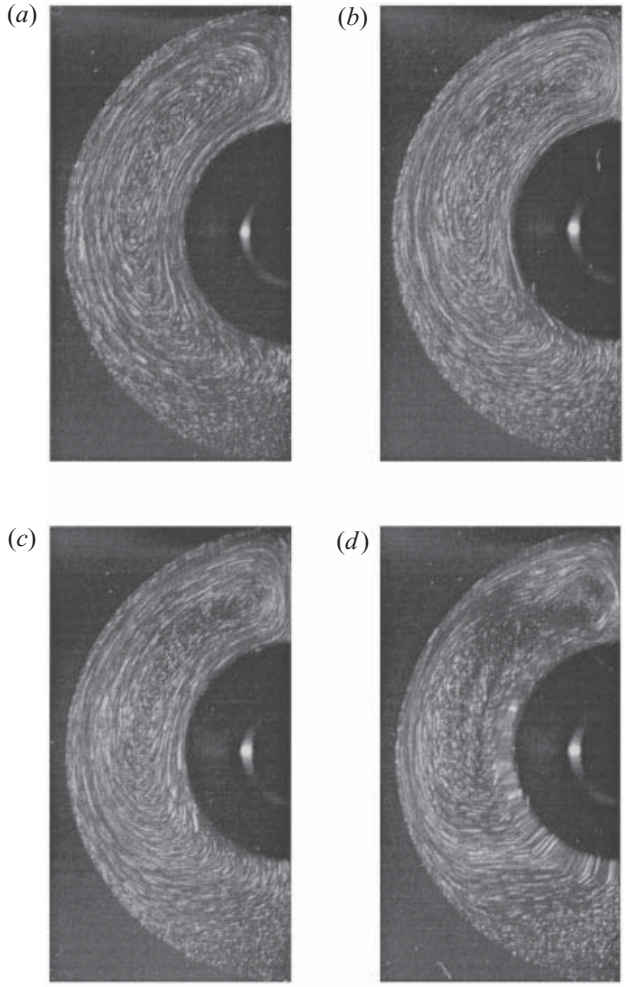

FIGURE 14. Experimental flow patterns at the mid-axial plane for $R = 2.1$, $L = 8.95$, $Pr = 100$: (*a*) $Ra = 8.725 \times 10^3$; (*b*) $Ra = 2.52 \times 10^4$; (*c*) $Ra = 4.36 \times 10^4$; (*d*) $Ra = 1.09 \times 10^5$.

5.3. *Large-gap annulus, large Prandtl number fluid*

Experiments were conducted to investigate flow patterns within an annulus of radius ratio $R = 2.1$ containing a silicone fluid with Prandtl number of 100. The Rayleigh number was successively increased from 8.725×10^3 to 1.09×10^5, which encompasses the range over which the stable crescent-shaped flow first changes to a steady unicellular pattern with rotational centre near $\phi = 0$, and then experiences transition to turbulence. Three-dimensional numerical simulations were performed to study the development of the corresponding temperature fields and obtain additional insight into the high Rayleigh number flow structure. The experimental and numerical investigations were both conducted for an annulus with a length of $L = 8.95$. A description of the experimental set-up is provided in §6.

A photograph of the steady state flow pattern at the mid-axial plane of the annulus for $Ra = 8.725 \times 10^3$ is presented in figure 14(*a*). In this view, a counter-clockwise rotating crescent-shaped recirculating flow is seen to be present. As the Rayleigh

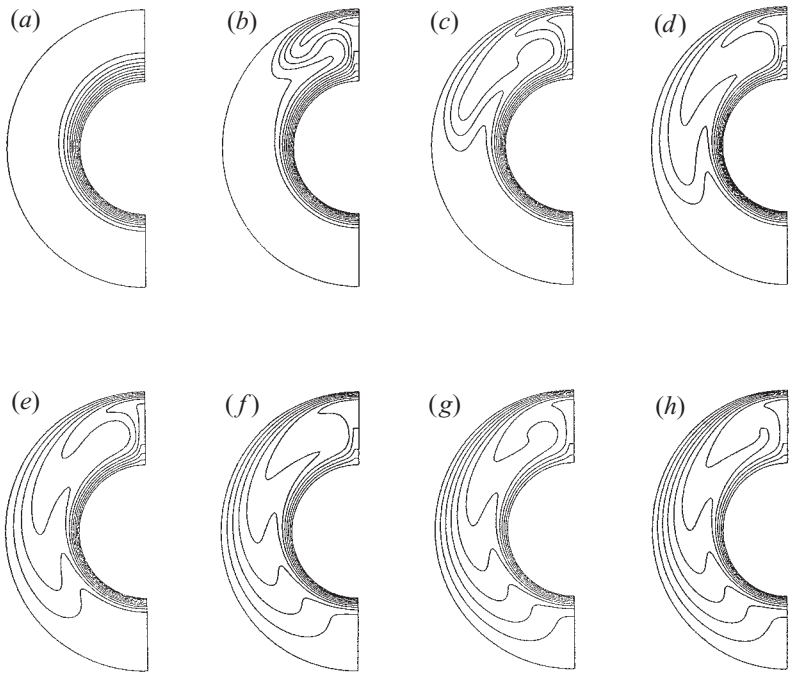

FIGURE 15. Temporal development of isotherms at the mid-axial plane for $Ra = 2.52 \times 10^4$, $R = 2.1$, $L = 8.95$, $Pr = 100$: (*a*) $t = 0.005$; (*b*) $t = 0.01$; (*c*) $t = 0.015$; (*d*) $t = 0.02$; (*e*) $t = 0.025$; (*f*) $t = 0.05$; (*g*) $t = 0.1$; (*h*) $t = 0.15$. Contours incremented by 0.1.

number is increased to 2.52×10^4, the flow changes to a steady unicellular pattern with the centre of rotation located within close proximity of the angular symmetry plane, as shown in figure 14(*b*). A small, elliptically shaped recirculation cell is located at the centre of rotation. Beneath this cell, a distinct boundary between the upward flow adjacent to the heated inner cylinder and the downward flow next to the cooled outer cylinder extends in the angular direction to approximately the location of the centre of rotation previously seen in figure 14(*a*) for $Ra = 8.725 \times 10^3$. With further increase in the Rayleigh number to 4.36×10^4 (figure 14*c*), the recirculation cell increases in size and a separation of streamlines appears immediately below the cell. This separation has not been reported in any previous investigation. The flow remains stable while the cell size continues to increase with Rayleigh number up to $Ra \approx 1 \times 10^5$, at which point the onset of turbulence is observed near the inner cylinder, as seen in figure 14(*d*), corresponding to a Rayleigh number of 1.09×10^5.

Three-dimensional numerical simulations were performed for $Ra = 8.725 \times 10^3$ and $Ra = 2.52 \times 10^4$. Comparison plots which illustrate the excellent agreement of experimental and numerical results are provided later on in figures 20 and 21. The calculated mean Nusselt numbers at the mid-axial plane corresponding to $Ra = 8.725 \times 10^3$ and $Ra = 2.52 \times 10^4$ are 2.20 and 2.92, respectively. At $Ra = 8.725 \times 10^3$, the isotherms within the approximate range of $\frac{1}{8}L < z < \frac{7}{8}L$ are constant with respect to axial position. At $Ra = 2.52 \times 10^4$, the temperature distribution is essentially invariant with respect to axial position over this same region except for minor changes in the vicinity of the recirculation cell which result from a slight weakening of the cell with closer proximity to the endwalls. These results indicate that the recirculation cell

in the top of the annulus is a cross-section of a longitudinal roll cell which extends over most of the annulus length. This was confirmed by examining the distribution of the z-component of vector potential at various axial planes. There is a total of two roll cells at the top of the annulus which are symmetric to each other about the vertical plane passing through the axis of the cylinders, and which rotate in the same directions as the symmetric main flow which surrounds each of them.

The temporal development of isotherms at the mid-axial plane resulting from sudden heating of the inner cylinder is shown in figure 15 for $Ra = 2.52 \times 10^4$. Up to the dimensionless time of $t = 0.005$, the isotherms appear as eccentric circles indicating that the strength of the flow is relatively weak and heat transfer is mainly by conduction. The streamline pattern shown in figure 21 becomes established at $t = 0.01$ which is reflected by the swirling pattern of isotherms in the top of the annulus (figure 15). The maximum value of the stream function at the mid-axial plane is attained at this time and remains constant as steady state conditions are achieved. The recirculating flow is strong enough to produce the inversion of isotherms seen in figures 15(*b*)–15(*h*) as the remaining fluid in the annulus is heated.

6. Comparison with experimental and previous numerical results

In addition to the previously described studies performed to ensure grid- and timestep-independent solutions, steady state numerical results for an annulus of $R = 2.6$ with air as the fluid medium were compared to those of Kuehn & Goldstein (1976) to verify the accuracy of the numerical scheme. Comparisons were made for Rayleigh numbers of $Ra = 10^3$ and $Ra = 10^4$. In both cases the streamlines, centre of flow rotation, and isotherms from our numerical model were found to be in excellent agreement with their results. The inner and outer cylinder Nusselt numbers reported by Kuehn & Goldstein (1976) were also compared with mid-axial plane Nusselt numbers from the present study, and the maximum difference was found to be less than 2%. In the present three-dimensional models, annuli of length $L = 10.4$ and $L = 20.8$ were modelled for the $Ra = 10^3$ and $Ra = 10^4$ cases, respectively, which resulted in two-dimensional flow at the mid-axis.

To further validate the three-dimensional numerical scheme and obtain additional information on flow stability, three sets of experiments were conducted, two with air and one with silicone fluid. Silicone fluid was used to obtain a high Prandtl number comparison. There is also no significant variation of thermophysical properties for temperatures between 10 °C and 100 °C. A brief description of each experimental set-up along with comparisons of the flow field photographic images and interferometer fringes to numerically calculated flow patterns and isotherms, respectively, are presented. In comparing the numerical results with the experimental data, the results are plotted to scale to cover the same display area as that of the experiment.

In the first experimental set-up using air, the inner and outer cylinder radii were 20 mm and 46 mm, respectively, resulting in a radius ratio of $R = 2.3$. The length of the test cell was 161 mm or a dimensionless length of $L = 8.05$. The inner and outer cylinders were maintained at hot and cold uniform temperatures, respectively, by means of heating and cooling jackets. Each of the endwalls was constructed of two layers of glass separated by a thin air space to simulate adiabatic boundaries. A thin transparent section was built into the annulus at the mid-axial position. To visualize the fluid motion, smoke was introduced into the annulus. The smoke particles were entrained by the fluid and were made visible by illuminating either the mid-axial plane or the upper angular symmetry plane with a thin sheet of light from a helium–neon

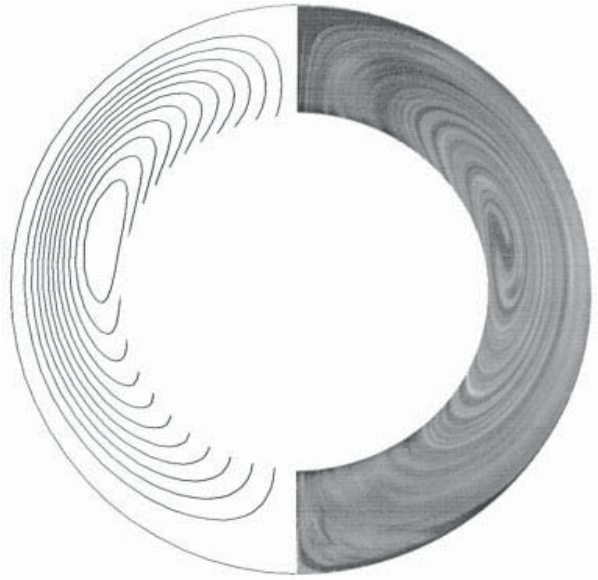

Numerical Experimental

FIGURE 16. Comparison of flow patterns at the mid-axial plane for $Ra = 3.32 \times 10^3$, $R = 2.3$, $Pr = 0.7$.

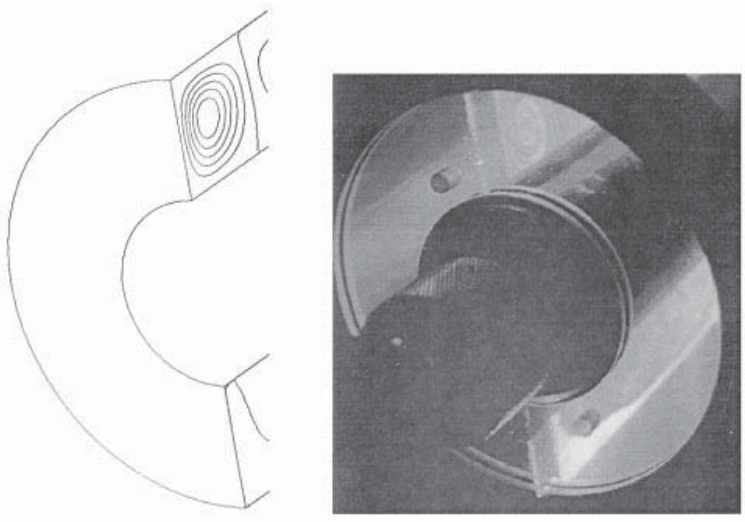

Numerical Experimental

FIGURE 17. Comparison of flow patterns at the upper angular symmetry plane for $Ra = 3.32 \times 10^3$, $R = 2.3$, $Pr = 0.7$.

laser. A comparison of the steady mid-axial plane flow pattern with computed results from the three-dimensional transient numerical simulation is given in figure 16 for $Ra = 3.32 \times 10^3$. The calculated streamlines in the left-half of the plot are seen to be in excellent agreement with the experimental flow visualization results on the right. The

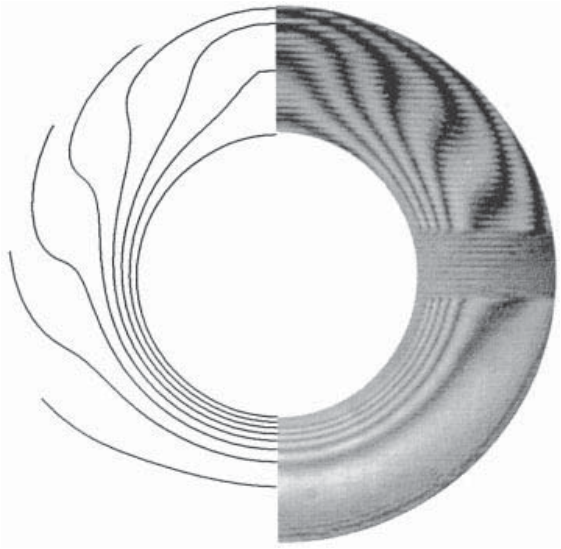

Numerical Experimental

FIGURE 18. Comparison of isotherms at the mid-axial plane for $Ra = 7.1 \times 10^3$, $R = 2.18$, $Pr = 0.7$.

calculated angular position of the centre of flow rotation is within 2% of the experimentally observed position. A perspective view of the smoke pattern in the upper angular symmetry plane of the annulus near the endwall is shown next to a plot of the calculated streamlines in figure 17. The primary flow feature in evidence in both the experimental and numerical results is a transverse vortex structure next to the endwall. The computed size and position of the vortex and the location of the vortex centre are seen to be in very good agreement with the experimental flow image. For both cases, the direction of rotation is counterclockwise.

The second experimental set-up using air was constructed so that a Mach–Zehnder interferometer could be used. The cell was 250 mm in length and the inner and outer radii were 11 mm and 24 mm, respectively, for $R = 2.18$ and $L = 22.7$. These sizes were chosen based on the dimensions of the interferometer. The light source was a helium–neon laser. Interferograms are shown in the right-halves of figures 18 and 19 for $Ra = 7.1 \times 10^3$ and $Ra = 1.1 \times 10^4$, respectively. The fringes can be considered as isotherms since the number of refraction is only a function of temperature. Steady state isotherms from the three-dimensional transient numerical simulation are plotted in the left-halves of the figures. For both Rayleigh numbers, the calculated isotherms are seen to compare very well with the experimental results. In these experiments, the investigated flow was found to be steady with no oscillations being observed until $Ra = 6.6 \times 10^4$, which is in good agreement with Kuehn & Goldstein (1976) and Powe *et al.* (1969).

In the third set of experiments, silicone fluid with a Prandtl number of 100 was employed. Flow visualization of the annular space was accomplished by transverse illumination of a single 5 mm wide cross-sectional plane, which was viewed from a longitudinal position through a glass end plate. The length of the cell was 340 mm and the inner and outer radii were 38 mm and 80 mm, respectively, for $R = 2.1$ and $L = 8.95$. The streamlines, made visible by seeding the fluid with alumine powder, are

Numerical Experimental

FIGURE 19. Comparison of isotherms at the mid-axial plane for $Ra = 1.1 \times 10^4$, $R = 2.18$, $Pr = 0.7$.

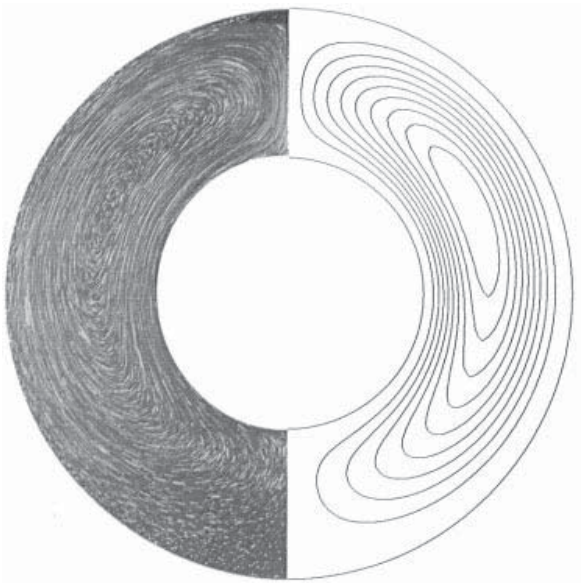

Experimental Numerical

FIGURE 20. Comparison of flow patterns at the mid-axial plane for $Ra = 8.725 \times 10^3$, $R = 2.1$, $Pr = 100$.

shown on the left-halves of figures 20 and 21 for $Ra = 8.725 \times 10^3$ and $Ra = 2.52 \times 10^4$, respectively. In the right-halves of these figures, steady-state streamlines at the mid-axial plane computed by the three-dimensional transient simulation are plotted. The agreement between experimental and numerical results is seen to be excellent. The

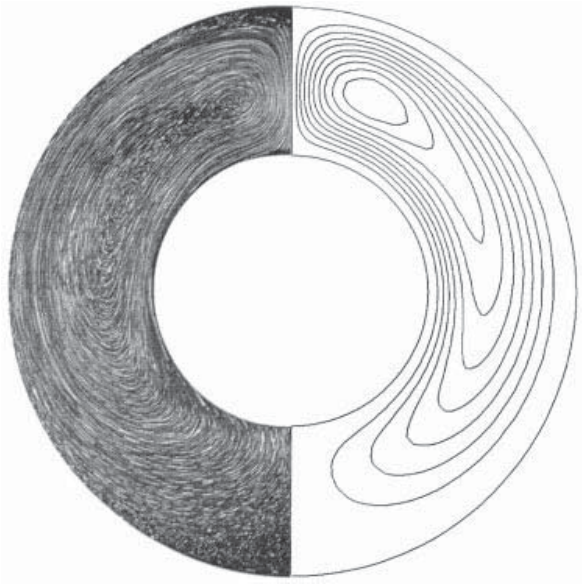

Experimental Numerical

FIGURE 21. Comparison of flow patterns at the mid-axial plane for $Ra = 2.52 \times 10^4$, $R = 2.1$, $Pr = 100$.

movement of the rotational centre of the flow into the upper part of the annulus, the recirculating cell located at the centre of rotation, and the boundary between upward and downward fluid movement extending below this cell in the angular direction are captured by the numerical model. The calculated angular positions of the centre of flow rotation for $Ra = 8.725 \times 10^3$ and $Ra = 2.52 \times 10^4$ are within 2° and 4°, respectively, of the experimentally observed positions. The flow remained steady as the Rayleigh number was increased up to approximately 1×10^5, at which point the onset of turbulence was observed near the inner cylinder surface.

7. Conclusions

A numerical investigation of the development of three-dimensional buoyancy-induced fluid flow and temperature fields with increasing Rayleigh number in moderate- and large-gap closed horizontal annuli has been conducted. The numerical results were shown to be in excellent agreement with results of the present experimental study. It has been shown for the first time that in a sufficiently long large-gap annulus containing air, three stable flow regions coexist at high Rayleigh numbers preceding transition to oscillatory flow. A three-dimensional recirculating flow consisting of a transverse vortex in the upper portion of the annulus and a double helical flow structure below this sets up next to each endwall. These end vortices, which were observed in the present numerical and experimental investigation, have not been identified in previous numerical or experimental studies. In the core region of the large-gap annulus centred on the mid-axial plane, the z-component of velocity is small and the thermal field retains the characteristics of that associated with two-dimensional flow. Between the endwall and core zones, a third region is distinguishable in which the primary flow circulation takes place in the (r, ϕ)-plane in conjunction with much lower

speed axial movement of fluid. These results confirm that in a large-gap annulus containing air, secondary flows do not arise in the core region of the annulus at Rayleigh numbers below that at which transition to oscillatory flow occurs.

A thorough three-dimensional study of buoyancy-driven flow in an air filled moderate-gap annulus has also been performed for the first time. It was shown that at low Rayleigh numbers the flow is very similar to that in a large-gap annulus, with two-dimensional crescent-type patterns present in the core region and a rotating end cell located in the upper portion of the annulus at each endwall. As the Rayleigh number is increased above Ra_L, however, an integral number of transverse spiral vortex pairs forms between the end vortices owing to thermal instability. The basic structure of the spiral flow and the Rayleigh number at which the full transition to spiral flow was calculated to occur agree very well with previous experimental results. The axial boundaries of the vortex structures define individual recirculating zones in which complex interactions between the primary and secondary flows take place. Fluid movement in the end vortex and inner vortex zones, which are distinctly different from each other in some respects, was described. The size of the inner vortical cells was shown to depend on the natural size predicted by the stability theory for an infinitely long annulus, the increase in Rayleigh number above the critical value, and the length of the annulus with solid endwalls into which an integral number of vortex pairs must fit in the space between end vortices. The temperature field and Nusselt number distribution in the upper portion of the annulus were shown to be significantly influenced by the presence of the vortex structures.

Results of a combined numerical and experimental investigation of natural convection within a large-gap annulus filled with a large Prandtl number fluid have been presented. It was shown that the crescent-shaped flow patterns present at low Rayleigh numbers progress to symmetric unicellular structures with centres of rotation near the top of the annulus as the Rayleigh number is increased. Longitudinal roll cells are positioned at the top of the annulus along the axial direction for higher Rayleigh number flows. As the Rayleigh number is increased further, a separation of streamlines appears below the cells. This result is presented for the first time. At an even higher Rayleigh number, transition to turbulence was observed to occur. Excellent agreement between the numerical results and those from the present experimental studies was shown, thereby verifying the accuracy of the numerical scheme.

The stability of two-dimensional buoyancy-induced flow between concentric horizontal cylinders was investigated using both linear theory and the energy method. A critical Rayleigh number $Ra_L(R)$ above which the flow is unstable was determined from the linear stability analysis. A subcritical Rayleigh number $Ra_E(R)$ which defines a necessary condition for global flow stability was obtained using the energy method. Below Ra_E, the two-dimensional flow is stable regardless of the perturbation amplitude. In the range $Ra_E < Ra < Ra_L$, the flow is stable for infinitely small perturbations and may be unstable for perturbations of a given amplitude. It was shown that both $Ra_L(R)$ and $Ra_E(R)$ tend to the value of 1708 as R approaches unity, which corresponds to the onset of natural convection in a horizontal layer, and that the $Ra_L(R)$ curve always lies above the $Ra_E(R)$ curve. The values of Ra_L obtained from the present study were shown to agree well with previously published results that are based on experimental observation.

One of the authors (K.V.) would like to thank the University of Paul Sabatier for inviting him several times over the past few years and providing the atmosphere conducive to joint research activities. The grant from the Ohio Supercomputer Center is also acknowledged and appreciated.

REFERENCES

Brian, P. L. T. 1961 A finite difference method of high-order accuracy for the solution of three-dimensional transient conduction problems. *AIChE J.* **7**, 367–370.

Cheddadi, A., Caltagirone, J. P., Mojtabi, A. & Vafai, K. 1992 Free two-dimensional convective bifurcation in a horizontal annulus. *Trans. ASME* C: *J. Heat Transfer* **114**, 99–106.

Choi, J. Y. & Kim, M. 1993 Three-dimensional linear stability of natural convective flow between concentric horizontal cylinders. *Intl J. Heat Mass Transfer* **36**, 4173–4180.

Davis, S. H. 1967 Convection in a box: linear theory. *J. Fluid Mech.* **30**, 465–478.

Desai, C. P. & Vafai, K. 1994 An investigation and comparative analysis of two- and three-dimensional turbulent natural convection in a horizontal annulus. *Intl. J. Heat Mass Transfer* **37**, 2475–2504.

Fant, D. B., Rothmayer, A., & Prusa, J. 1991 Natural convective flow instability between horizontal concentric cylinders. *J. Thermophys.* **3**, 407–414.

Fusegi, T. & Farouk, B. 1986 A three-dimensional study of natural convection in the annulus between horizontal concentric cylinders. In *Proc. 8th Intl Heat Transfer Conf.* vol. 4, pp. 1575–1580.

Grigull, U. & Hauf, W. 1966 Natural convection in horizontal cylindrical annuli. In *Proc. 3rd Intl Heat Transfer Conf.* vol. 2, pp. 182–195.

Hirasaki, G. J. & Hellums, J. D. 1968 A general formulation of the boundary conditions on the vector potential in three-dimensional hydrodynamics. *Q. Appl. Math.* **26**, 331–342.

Kuehn, T. H. & Goldstein, R. J. 1976 An experimental and theoretical study of natural convection in the annulus between horizontal concentric cylinders. *J. Fluid Mech.* **74**, 695–719.

Liu, C., Mueller, W. K. & Landis, F. 1961 Natural convection heat transfer in long horizontal cylindrical annuli. *International Developments in Heat Transfer*, Part V, pp. 976–984.

Mojtabi, A. & Caltagirone, J. P. 1979 Energy stability of a natural convective flow in a horizontal annular space. *Phys. Fluids* **22**, 1208–1209.

Powe, R. E., Carley, C. T. & Bishop, E. H. 1969 Free convective flow patterns in cylindrical annuli. *Trans. ASME* C: *J. Heat Transfer* **91**, 310–314.

Powe, R. E., Carley, C. T. & Carruth, S. L. 1971 A numerical solution for natural convection in cylindrical annuli. *Trans. ASME* C: *J. Heat Transfer* **93**, 210–220.

Rao, Y. F., Miki, Y., Fukuda, K., Takata, Y. & Hasegawa, S. 1985 Flow patterns of natural convection in horizontal cylindrical annuli. *Intl. J. Heat Mass Transfer* **28**, 705–714.

Stork, K. & Muller, U. 1972 Convection in boxes: experiments. *J. Fluid Mech.* **54**, 599–611.

Takata, Y., Iwashige, K., Fukuda, K. & Hasegawa, S. 1984 Three-dimensional natural convection in an inclined cylindrical annulus. *Intl J. Heat Mass Transfer* **27**, 747–754.

Vafai, K. & Ettefagh, J. 1991 An investigation of transient three-dimensional buoyancy-driven flow and heat transfer in a closed horizontal annulus. *Intl J. Heat Mass Transfer* **34**, 2555–2570.

Walton, I. C. 1980 The stability of free convection in a horizontal cylindrical annulus. *Q. J. Mech. Appl. Maths* **33**, 125–139.

Yoo, J. S. 1996 Dual steady solutions in natural convection between horizontal concentric cylinders. *Intl J. Heat Fluid Flow* **17**, 587–593.